

# The Properties of the Interstellar Medium within a Star-Forming Galaxy at $z=2.3$

A. L. R. Danielson,<sup>1,\*</sup> A. M. Swinbank,<sup>1</sup> Ian Smail,<sup>1</sup> P. Cox,<sup>2</sup> A. C. Edge,<sup>1</sup> A. Weiss,<sup>3</sup> A. I. Harris,<sup>4</sup> A. J. Baker,<sup>5</sup> C. De Breuck,<sup>6</sup> J. E. Geach,<sup>1</sup> R. J. Ivison,<sup>7,8</sup> M. Krips,<sup>2</sup> A. Lundgren,<sup>9</sup> S. Longmore,<sup>10</sup> R. Neri,<sup>2</sup> & B. Ocaña Flaquer,<sup>11</sup>

<sup>1</sup>*Institute for Computational Cosmology, Department of Physics, Durham University, South Road, Durham DH1 3LE, UK*

<sup>2</sup>*Institut de Radio Astronomie Millimétrique, 300 rue de la Piscine, Domaine Universitaire, 38406 Saint Martin d'Heres, France*

<sup>3</sup>*Max-Planck Institut für Radioastronomie, Auf dem Hügel 69, 53121 Bonn, Germany*

<sup>4</sup>*Department of Astronomy, University of Maryland, College Park, Maryland 20742, USA*

<sup>5</sup>*Department of Physics and Astronomy, Rutgers, the State University of New Jersey, 136 Frelinghuysen Road, Piscataway, New Jersey 08854-8019, USA*

<sup>6</sup>*European Southern Observatory, Karl-Schwarzschild Strasse, 85748 Garching bei München, Germany*

<sup>7</sup>*UK Astronomy Technology Centre, Royal Observatory, Blackford Hill, Edinburgh, EH19 3HJ, UK*

<sup>8</sup>*Institute for Astronomy, University of Edinburgh, Edinburgh, EH19 3HJ, UK*

<sup>9</sup>*European Southern Observatory, Alonso de Cordova 3107, Cassilla 19001, Santiago 19, Chile*

<sup>10</sup>*Harvard-Smithsonian Center For Astrophysics, 60 Garden Street, Cambridge, Massachusetts 02138, USA*

<sup>11</sup>*Instituto de Radioastronomía Milimétrica, Avenida Divina Pastora 7, Núcleo Central, 18012 Granada, Spain*

\*Email: a.l.r.danielson@durham.ac.uk

29 September 2018

## ABSTRACT

We present an analysis of the molecular and atomic gas emission in the rest-frame far-infrared and sub-millimetre, from the lensed  $z = 2.3$  sub-millimetre galaxy SMM J2135–0102. We obtain very high signal-to-noise detections of 11 transitions from three species and limits on a further 20 transitions from nine species. We use the  $^{12}\text{CO}$ , [C I] and HCN line strengths to investigate the gas mass, kinematic structure and interstellar medium (ISM) chemistry, and find strong evidence for a two-phase medium within this high-redshift starburst galaxy, comprising a hot, dense, luminous component and an underlying extended cool, low-excitation massive component. Employing a suite of photo-dissociation region models we show that on average the molecular gas is exposed to a UV radiation field that is  $\sim 1000\times$  more intense than the Milky Way, with star-forming regions having a characteristic density of  $n \sim 10^4 \text{ cm}^{-3}$ . Thus, the average ISM density and far-UV radiation field intensity are similar to those found in local ULIRGs. These densities and radiation fields are similar to those found in the central regions of typical starburst galaxies, even though the star formation rate is far higher in this system. The  $^{12}\text{CO}$  spectral line energy distribution and line profiles give strong evidence that the system comprises multiple kinematic components with different conditions, including temperature, and line ratios suggestive of high cosmic ray flux within clouds, likely as a result of high star formation density. We find tentative evidence of a factor  $\sim 4$  temperature range within the system. We expect that such internal structures are common in high-redshift ULIRGs but are missed due to the poor signal-to-noise of typical observations. We show that, when integrated over the galaxy, the gas and star-formation surface densities appear to follow the Kennicutt-Schmidt relation, although by comparing our data to high-resolution sub-mm imaging, our data suggest that this relation breaks down on scales of  $<100 \text{ pc}$ . By virtue of the lens amplification, these observations uncover a wealth of information on the star formation and ISM at  $z \sim 2.3$  at a level of detail that has only recently become possible at  $z < 0.1$ , and show the potential physical properties that will be studied in unlensed galaxies when the Atacama Large Millimeter Array is in full operation.

**Key words:** galaxies: active — galaxies: evolution — galaxies: high-redshift — galaxies: starburst — sub-millimetre

## 1 INTRODUCTION

The properties of the interstellar medium (ISM) play a critical role in the evolution of galaxies as it includes the raw material from which stars form. The main sources of heating of the atomic and molecular ISM are the stellar radiation field, cosmic rays and turbulence, and as such the ISM exhibits a considerable range of properties, spanning a wide range in density  $\sim 10^{0-7} \text{ cm}^{-3}$  and temperature  $\sim 10\text{--}1000 \text{ K}$ . The thermodynamic state of the gas is dictated by the balance of this heating with cooling from atomic and molecular species (e.g. [CII], [CI],  $^{12}\text{CO}$  and [OI]) and this balance may dictate the Jeans mass and initial mass function (IMF) and therefore the efficiency of star formation (Hocuk & Spaans 2010). Understanding the balance of heating and cooling within the ISM is thus fundamental to understanding the detailed physics of the star formation which drives the formation and evolution of galaxies.

An essential element of our understanding of distant galaxies comes therefore from observations of emission from interstellar molecular and atomic gas. To date, the majority of the detections of  $^{12}\text{CO}$  and atomic fine structure emission from high-redshift galaxies have been in powerful QSOs and intrinsically luminous galaxies, typically with star formation rates  $> 10^3 \text{ M}_\odot \text{ yr}^{-1}$  (e.g. Frayer et al. 1998, 1999; Greve et al. 2005; Tacconi et al. 2006, 2008; Hailey-Dunsheath et al. 2010a; Walter et al. 2009). However, the detailed physical properties of the vigorous starbursts within high-redshift starburst galaxies are still unknown. Analogy to local ultra-luminous infrared galaxies (ULIRGs) would argue for compact starbursts triggered by mergers, although secular bursts in massive gas disks are also feasible (e.g. Davé et al. 2010). These different scenarios imply different properties for the ISM and so may be tested using observations of the molecular and atomic emission. Critically, the first full  $^{12}\text{CO}$  spectral line energy distributions (SLEDs), including high- $J_{\text{upper}}$  transitions, have recently been completed for local ULIRGs (Papadopoulos et al. 2010; van der Werf et al. 2010) providing an empirical benchmark for comparison to high-redshift sources, to search for similarities in the thermodynamics of their ISM.

Much of the atomic and molecular gas emission from galaxies arises from photo-dissociation regions (PDRs), the surfaces of molecular clouds where the heating and chemistry is dominated by far-ultraviolet (far-UV) photons from stellar sources (Hollenbach & Tielens 1997). PDRs dominate the infrared and sub-millimetre emission line spectra of star formation regions and galaxies as a whole. The majority of their cooling occurs via atomic fine structure lines of [OI], [CII] and the rotational  $^{12}\text{CO}$  lines (Kramer et al. 2004).

Prior to full science operations of ALMA, the most promising route to gaining high signal-to-noise, sub-millimetre spectroscopy of star-forming galaxies at high redshift is to use the natural amplification from strong gravitational lensing (e.g. Smail et al. 2002; Weiß et al. 2005, 2007; Maiolino et al. 2009; Hailey-Dunsheath et al. 2010a; Ivison et al. 2010). In particular, measuring the chemistry of the ISM through emission line flux ratios in strongly-lensed galaxies is particularly advantageous since gravitational lensing is achromatic (in the absence of differential amplification) and so the apparent line ratios (and the im-

plied chemistry) are unaffected. As such, intrinsically faint emission lines which are sensitive probes of the ISM chemistry (such as  $^{13}\text{CO}$  or HCN) can be measured, if suitably bright targets can be identified.

Recently, Swinbank et al. (2010) reported the discovery of a strongly-lensed sub-millimetre galaxy SMM J2135–0102 (hereafter SMM J2135; R.A./Dec.: 21 35 11.6, –01 02 52; J2000) behind a massive galaxy cluster at  $z = 0.325$ . The redshift for the galaxy,  $z = 2.3259$ , was derived through blind detection of  $^{12}\text{CO}(1\text{--}0)$  using Zpectrometer on Green Bank Telescope (GBT). Based on a detailed lensing model, the  $870\text{-}\mu\text{m}$  emission appears to be amplified by a factor  $32.5 \pm 4.5\times$ , implying an unlensed flux density of  $\sim 3 \text{ mJy}$  ( $L_{\text{bol}} = 2.3 \pm 0.4 \times 10^{12} \text{ L}_\odot$ ; Ivison et al. 2010), which is close to the confusion limit of existing sub-millimetre surveys (Blain et al. 2002).

This uniquely bright source therefore provides an opportunity to investigate the detailed properties of the ISM within a galaxy which is representative of the high-redshift starburst population. In this paper we analyse follow-up observations of the  $^{12}\text{CO}$  ladder (up to  $J_{\text{upper}} = 10$ ), as well as other dense gas tracers and more complex molecules in the rest-frame frequency range  $80\text{--}1100 \text{ GHz}$ . To put the current molecular/atomic line data obtained for the *global* line emission of this distant starburst in perspective, we note that they are rivaled only by those obtained for local ULIRGs, e.g. Arp 220, Mrk 231 and NGC 6240 (Greve et al. 2009; van der Werf et al. 2010), which are some  $\sim 250\times$  closer to us.

In §2 we describe our observations of the molecular and atomic emission from SMM J2135. Our analysis is described in §3 where we first examine the integrated properties of the system, deriving and comparing gas masses calculated from  $^{12}\text{CO}$ , [CI] and HCN. We produce a  $^{12}\text{CO}$  SLED for this galaxy and use this to investigate excitation conditions within its ISM. We use PDR models to investigate the characteristic density of the ISM and the incident far-UV intensity. We then decompose the spectra into three distinct kinematic components, and measure the  $^{12}\text{CO}$  SLED of each in order to search for excitation structure within the system. We give our conclusions in §4. Throughout the paper we use a  $\Lambda\text{CDM}$  cosmology with  $H_0 = 72 \text{ km s}^{-1} \text{ Mpc}^{-1}$ ,  $\Omega_m = 0.27$  and  $\Omega_\Lambda = 1 - \Omega_m$  (Spergel et al. 2003). Unless otherwise stated, a lensing amplification correction of a factor of 32.5 has already been applied to all quoted luminosities.

## 2 OBSERVATIONS

An essential requirement for the study of the molecular and atomic emission lines from SMM J2135 is a precise redshift for the gas reservoir in this system. This was obtained soon after the discovery of the source using Zpectrometer on GBT (Swinbank et al. 2010, see §2.1). With this accurate systemic redshift, it was then possible to precisely tune to the expected frequencies of molecular and atomic emission lines.

### 2.1 GBT Zpectrometer Observations

Details of the observations with Zpectrometer are given in Swinbank et al. (2010) and Table 1. Briefly, Zpectrometer is a wide-band spectrometer optimised for  $^{12}\text{CO}(1\text{--}0)$  emission

TABLE 1.  
LOG OF IRAM 30 M AND GBT OBSERVATIONS

Band	$\nu_{\text{obs}}$ (GHz)	Emission lines	$t_{\text{int}}$ (ks)
Ka	25.6–36.1	$^{12}\text{CO}(1-0)$ , $\text{CS}(2-1)$ , $\text{CN}(1-0)$	
		$\text{HNC}(1-0)$ , $^{13}\text{CO}(1-0)$	
		$\text{HCO}^+(1-0)$	18.0
E0	79.00–83.00	$\text{HCN}(3-2)$ , $\text{HCO}^+(3-2)$ ,	
		$\text{HNC}(3-2)$	28.8
	96.75–100.75	$^{13}\text{CO}(3-2)$ , $\text{H}_2\text{O } 325.141$	18.0
	101.97–105.97	$^{12}\text{CO}(3-2)$ , $\text{CN}(3-2)$ , $\text{CS}(7-6)$	18.0
E1	131.00–135.00	$^{13}\text{CO}(4-3)$ , $\text{HCO}^+(5-4)$ ,	
		$\text{HCN}(5-4)$ , $\text{CS}(9-8)$	14.4
	135.92–139.92	$^{12}\text{CO}(4-3)$ , $\text{CN}(4-3)$ , $\text{HNC}(5-4)$	10.8
	146.00–150.00	$[\text{C}]\text{I}(1-0)$ , $\text{CS}(10-9)$ , $\text{O}_2 487.3$	7.2
	171.26–174	$^{12}\text{CO}(5-4)$	10.8
E2	205.90–209.90	$^{12}\text{CO}(6-5)$	8.4
	224.11–228.11	$\text{H}_2\text{O } 731.681$	3.6
	240.53–244.53	$^{12}\text{CO}(7-6)$ , $[\text{C}]\text{I}(2-1)$	12.6
E3	275.16–279.16	$^{12}\text{CO}(8-7)$	9.6
	309.77–313.77	$^{12}\text{CO}(9-8)$	7.2

The log of the IRAM 30m and GBT Zpectrometer observations giving the frequency ranges of Zpectrometer Ka band and the IRAM/EMIR receiver backends (E0–E3), the emission lines observed and integration time for each set-up.

Note: These set-ups have beam sizes of Ka: $\sim 15''$ – $23''$ , E0: $\sim 30''$ , E1: $\sim 17''$ , E2: $\sim 11''$  and E3: $\sim 8.5''$  respectively.

line searches between  $z = 2.2$ – $3.5$  (with  $\sim 150 \text{ km s}^{-1}$  resolution) using the GBT’s Ka-band receiver (see Harris et al. 2007 and Harris et al. 2010 for more detail on the instrument and observing mode). Observations of SMM J2135 were conducted in two equal shifts on 2009 May 19 and May 27 for a total integration time of 5 hours. Data reduction was carried out with the standard Zpectrometer GBT reduction scripts. The final spectrum reaches an rms noise level of  $\sigma = 0.50 \text{ mJy beam}^{-1}$ . From the spectrum, shown in Fig. 1, we determine the heliocentric redshift as  $z = 2.32591$  from the  $^{12}\text{CO}(1-0)$  emission at 34.648 GHz. The observed velocity-integrated flux in  $^{12}\text{CO}(1-0)$  is given in Table 2.

## 2.2 IRAM PdBI & 30m Observations

We used the six-element IRAM Plateau de Bure Interferometer (PdBI) to observe the redshifted  $^{12}\text{CO}(3-2)$  and  $^{12}\text{CO}(4-3)$  emission lines and the continuum at 104 GHz and 139 GHz respectively. Observations were made in D configuration in Directors Discretionary Time (DDT) on 2009 May 29 and 31 with good atmospheric phase stability and precipitable water vapour (seeing =  $0.6$ – $1.6''$ , pwv =  $5$ – $15 \text{ mm}$ ). The receivers were tuned to the systemic redshift determined from the GBT  $^{12}\text{CO}(1-0)$  spectrum. We observed SMM J2135 for total on-source exposure times of 4 hrs and 2 hrs for  $^{12}\text{CO}(3-2)$  and  $^{12}\text{CO}(4-3)$  respectively. The correlator was adjusted to a frequency resolution of 2.5 MHz, yielding 980-MHz coverage. The overall flux scale for each observing epoch was set from observations of MWC 349, with additional observations of 2134+004 for phase and amplitude calibrations. The data were calibrated, mapped and

TABLE 2.  
EMISSION LINE PROPERTIES

Species	$\nu_{\text{rest}}$ (GHz)	Flux <sup>a,b</sup> (Jy $\text{km s}^{-1}$ )	L' ( $10^8 \text{ K km s}^{-1} \text{ pc}^2$ )
$^{12}\text{CO}(1-0)$	115.2712	$2.16 \pm 0.11$	$173 \pm 9$
$^{12}\text{CO}(3-2)$	345.7959	$13.20 \pm 0.10$	$117.6 \pm 0.9$
$^{12}\text{CO}(4-3)$	461.0408	$17.3 \pm 1.2$	$87 \pm 6$
$^{12}\text{CO}(5-4)$	576.2679	$18.7 \pm 0.8$	$60 \pm 3$
$^{12}\text{CO}(6-5)$	691.4731	$21.5 \pm 1.1$	$48 \pm 2$
$^{12}\text{CO}(7-6)$	806.6518	$12.6 \pm 0.6$	$21 \pm 1$
$^{12}\text{CO}(8-7)$	921.7997	$8.8 \pm 0.5$	$11 \pm 1$
$^{12}\text{CO}(9-8)$	1036.9124	$3.6 \pm 1.7$	$4 \pm 2$
$^{12}\text{CO}(10-9)$	1151.9855	$< 1.1$	$< 0.9$
$^{13}\text{CO}(1-0)$	110.2013	$< 0.3$	$< 29$
$^{13}\text{CO}(3-2)$	330.5880	$< 1.8$	$< 18$
$^{13}\text{CO}(4-3)$	440.7651	$< 0.3$	$< 1.4$
$[\text{C}]\text{I}(1-0)$	492.1607	$16.0 \pm 0.5$	$71 \pm 2$
$[\text{C}]\text{I}(2-1)$	809.3435	$16.2 \pm 0.6$	$26 \pm 1$
$\text{HCN}(1-0)$	88.6300	$< 0.3$	$< 45$
$\text{HCN}(3-2)$	265.8900	$1.2 \pm 0.4$	$18 \pm 6$
$\text{HCN}(5-4)$	443.1200	$< 0.3$	$< 1.4$
$\text{HNC}(1-0)$	90.6600	$< 0.3$	$< 43$
$\text{HNC}(3-2)$	271.9800	$< 1.2$	$< 17$
$\text{HCO}^+(1-0)$	89.190	$< 0.3$	$< 44$
$\text{HCO}^+(3-2)$	267.560	$< 1.2$	$< 17$
$\text{HCO}^+(5-4)$	445.90	$< 0.3$	$< 1.3$
$\text{CN}(1-0)$	113.320	$< 0.3$	$< 27$
$\text{CN}(3-2)$	339.450	$< 1.6$	$< 14$
$\text{CS}(2-1)$	97.981	$< 0.3$	$< 37$
$\text{CS}(7-6)$	342.883	$< 1.6$	$< 14$
$\text{CS}(9-8)$	428.875	$< 0.3$	$< 14$
$\text{CS}(10-9)$	489.751	$< 1.6$	$< 7$
$\text{O}_2$	487.246	$< 1.6$	$< 7$
$\text{H}_2\text{O}$	325.141	$< 1.8$	$< 18$
$\text{H}_2\text{O}$	731.681	$< 4.8$	$< 9.5$
$[\text{C}]\text{II}^c$	1910	$850 \pm 180$	$2500 \pm 500$
$[\text{O}]\text{I}^d$	2065.40	$620 \pm 200$	$155 \pm 50$

<sup>a</sup>We quote  $3\sigma$  limits for all lines which are not formally detected.

<sup>b</sup>Uncertainties on fluxes denote measurement errors and do not include the calibration uncertainties, which we estimate as  $\sim 5\%$  for 30–200 GHz,  $\sim 10\%$  for 200–300 GHz and  $\sim 15\%$  for  $> 300$  GHz.

<sup>c</sup>The  $[\text{C}]\text{II}$  flux is taken from Ivison et al. (2010).

<sup>d</sup>Ivison et al. (2010) report a  $\sim 3\sigma$  from  $[\text{O}]\text{I} 146\mu\text{m}$  and we have used the flux of this feature in our analysis, although we note that removing this line from our analysis changes our results negligibly. We also note that the since the  $[\text{C}]\text{II}$  and  $[\text{O}]\text{I} 146\mu\text{m}$  lines are of comparable strength, this would imply that the  $[\text{O}]\text{I} 63\mu\text{m}$  line would be much brighter than the  $[\text{C}]\text{II}$  line thus making this an interesting source for Herschel/PACS follow-up.

analyzed using the GILDAS software package. Inspection of the velocity datacubes shows very good detections of both  $^{12}\text{CO}(3-2)$  and  $^{12}\text{CO}(4-3)$  emission lines ( $\text{S/N} \sim 300$  in each) at the position of SMM J2135 (see Fig. 1) and we give line fluxes in Table 2.

To constrain the high- $J_{\text{upper}}$   $^{12}\text{CO}$  emission (and search for other emission lines such as  $[\text{C}]\text{I}$ ) we used the Eight MIXer Receiver (EMIR) multi-band heterodyne receiver at the IRAM 30-m telescope. Observations were made on 2009

June 29–30, and 2010 February 5–8 and April 3–6, in good to excellent conditions, typically with  $\sim 2\text{--}6\text{ mm}$  pwv and  $\lesssim 1\text{ mm}$  pwv for some of the April observations. Data were recorded using the E0–E3 receivers with 4 GHz of instantaneous, dual-polarisation band-width covering frequency ranges from  $\sim 70\text{--}310\text{ GHz}$  (see Table 1 for the details of the setups). For each observation, we used eight 1-GHz band-width units of the Wide-band Line Multiple Autocorrelator (WILMA) to cover 4 GHz in both polarizations. WILMA provides a spectral resolution of 2 MHz which corresponds to  $5\text{--}7\text{ km s}^{-1}$  in the 3-mm band. The observations were carried out in wobbler-switching mode, with a switching frequency of 1 Hz and an azimuthal wobbler throw of  $90''$ . Pointing was checked frequently on either the nearby quasar J2134+004 or Venus and was found to be stable to within  $3''$ . Calibration was carried out every 12 mins using the standard hot/cold-load absorber, and the flux calibration was carried out using the point source conversion between temperature and flux as measured from celestial objects. We note that, even at the highest frequency (i.e. 345 GHz) the beam is  $8.5''$  and so the lensed galaxy is likely to be smaller than the beam at all wavelengths (Swinbank et al. 2010). The data were first processed with the CLASS software (Pety 2005), and then using custom IDL routines. We omitted scans with distorted baselines and subtracted only linear baselines from individual spectra. For the 2010 April observations of  $^{12}\text{CO}(5\text{--}4)$ , an upward correction was made to the flux of 10% since the line extends into the wings of an atmospheric water band (although for these observations the pwv  $\lesssim 1\text{ mm}$ ). In total, we observed twelve different set-ups, each for  $\sim 2\text{--}5\text{ hrs}$  (Table 1); the spectra of the detections are shown in Fig. 1. These observations provide detections or limits on 31 transitions listed in Table 2.

### 2.3 APEX SHFI Observations

Observations of the redshifted  $^{12}\text{CO}(7\text{--}6)$  emission line were also carried out in DDT using the Swedish Heterodyne Facility Instrument (SHFI) between 2009 July 10 and July 20 (ESO programme ID 283.A-5014). SHFI consists of four wide-band heterodyne receiver channels for 230–1300 GHz (Vassilev et al. 2008). We used APEX-1 tuned at 242.4 GHz to search for the  $^{12}\text{CO}(7\text{--}6)$  emission from the galaxy, and obtained a total integration time of  $\sim 5.5\text{ hrs}$  in excellent conditions ( $0.4\text{--}0.6\text{ mm}$  pwv). The data reduction was carried out using the CLASS software, omitting scans with poor baselines. To create the final spectrum we binned the data onto a velocity scale of  $50\text{ km s}^{-1}$  and averaged it together with 4 hours of observations from IRAM/EMIR, which has similar signal-to-noise; we show this spectrum in Fig. 1.

### 2.4 SMA Observations

We mapped the  $870\text{-}\mu\text{m}$  continuum emission from SMM J2135 using the Submillimeter Array (SMA) in a number of different array configurations (see Swinbank et al. 2010). During four of these tracks (in the sub-compact, compact, extended and very-extended configurations) we tuned the upper side band of the receiver to 346.36699 GHz to search for  $^{12}\text{CO}(10\text{--}9)$ . Details of the data reduction are given in Swinbank et al. (2010) and we show the spectrum

in Fig. 1. The resulting combined spectrum reaches an rms of  $2\text{ mJy}$  per  $100\text{ km s}^{-1}$  channel and although  $^{12}\text{CO}(10\text{--}9)$  is not detected, we place a  $3\text{-}\sigma$  limit on the flux of  $\leq 0.2\text{ Jy km s}^{-1}$ .

## 3 ANALYSIS AND DISCUSSION

Our observations have detected 11 individual transitions arising from three molecular or atomic species in SMM J2135 and place upper limits on the line fluxes of a further 20 transitions arising from seven other species. We list these in Table 2 with the fluxes quoted with their respective measurement uncertainties and we show the spectra for all detections in Fig. 1. We estimate additional calibration uncertainties of 5%, 10% and 15% for those lines at 30–200 GHz, 200–300 GHz and  $> 300\text{ GHz}$  respectively.

With the very high signal-to-noise of our data (particularly the  $^{12}\text{CO}$  lines), we clearly identify multiple velocity components within the spectra (at approximately  $-180, 0$  and  $+200\text{ km s}^{-1}$  relative to the  $^{12}\text{CO}(1\text{--}0)$  flux-weighted mean velocity), implying multiple physical components in the source. We believe that the detection of this structure in the  $^{12}\text{CO}$  spectra is not due to this galaxy's being unusual, but instead reflects the high signal-to-noise of our observations, which is uncommon for observations of other (even local) galaxies. We discuss these multiple components in §3.3, modelling the system as three components which we label X, Y and Z. However, so that fair comparisons can be made to other galaxies (at low and high redshift), we begin (in §3.1.1, 3.1.2 and 3.2) by discussing the integrated properties of the system to see what can be learnt about the bulk properties of its ISM.

As Fig. 1 shows, the  $^{12}\text{CO}$  and [C I] emission lines are broad, with a typical FWHM of  $\sim 500\text{ km s}^{-1}$ . Since there is significant kinematic structure within the  $^{12}\text{CO}$  and [C I] emission, we first define the width of the emission lines by constructing a composite  $^{12}\text{CO}$  spectrum by combining the spectra from  $^{12}\text{CO}(1\text{--}0)$  to  $^{12}\text{CO}(8\text{--}7)$  (normalised by peak flux). This composite has a full width at zero intensity of  $900\text{ km s}^{-1}$ , with a range from  $-350$  to  $550\text{ km s}^{-1}$  (Fig. 1), although we note that there may be faint emission extending to  $\pm 1000\text{ km s}^{-1}$ . We use the velocity range,  $-350$  to  $550\text{ km s}^{-1}$ , to measure the fluxes of the  $^{12}\text{CO}$  lines, [C I]( $^3P_1 \rightarrow ^3P_0$ ) and [C I]( $^3P_2 \rightarrow ^3P_1$ ), while for HCN( $3\text{--}2$ ) we use a range of  $-100$  to  $550\text{ km s}^{-1}$ . To determine the errors on the fluxes we measure the variance in the spectra away from the emission line, although in most cases the dominant error is from the calibration; these errors are used in Fig. 2 (see also Table 2).

### 3.1 Integrated Properties

#### 3.1.1 Gas Mass and Dust SED

We begin by estimating the total molecular gas mass of the galaxy from  $^{12}\text{CO}$ . Low- $J_{\text{upper}}$  transitions of  $^{12}\text{CO}$  are commonly used to obtain estimates of the total gas mass of a galaxy using a conversion factor,  $\alpha = M_{\text{H}_2} / L'_{^{12}\text{CO}(1\text{--}0)} M_{\odot} (\text{K km s}^{-1} \text{ pc}^2)^{-1}$  which converts the  $^{12}\text{CO}$  line luminosity to total gas mass, (where  $M_{\text{H}_2}$  is

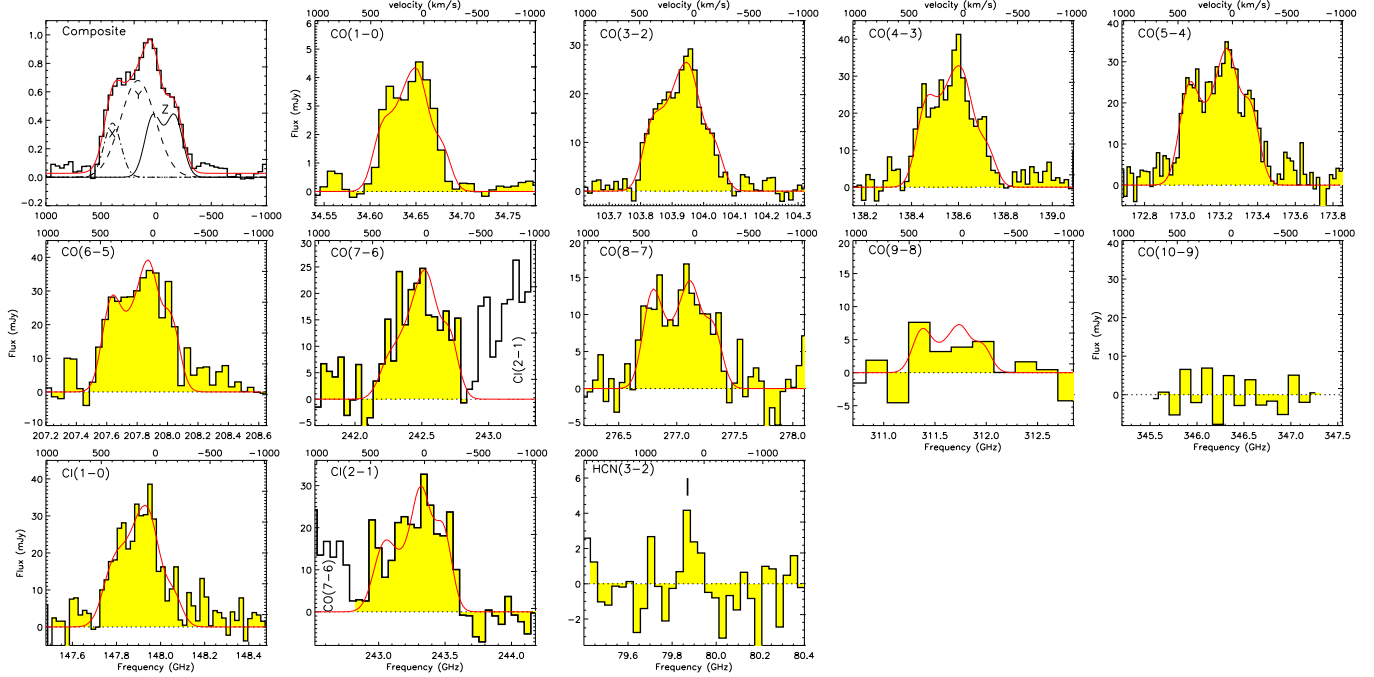


**Figure 1.** Molecular and atomic emission from the lensed sub-millimetre galaxy SMM J2135. The top two rows show spectra of the  $^{12}\text{CO}$  emission arising from  $J_{\text{upper}} = 1$  up to  $J_{\text{upper}} = 10$ . These are followed by the spectra of the [C I] fine-structure lines and our detection of HCN(3–2). In all cases, the emission profiles show multiple velocity components whose intensity appears to vary between transitions. To better constrain the kinematic structure of the lines we derive an average  $^{12}\text{CO}$  spectrum (which does not include  $^{12}\text{CO}(9-8)$  or  $^{12}\text{CO}(10-9)$ ) and we overplot on this the resulting three-component parametric model as described in §3.3. We fit this three-component kinematic model to the various lines, allowing the intensities of the components to vary between lines, and overlay this on all the  $^{12}\text{CO}$  emission lines making up the average, clearly highlighting the evidence of different excitation in the different velocity components. The spectra have been binned into channels of width 30–100 km s $^{-1}$ . The spectra for  $^{12}\text{CO}(3-2)$ ,  $^{12}\text{CO}(4-3)$  and  $^{12}\text{CO}(6-5)$  are the combined data from our PdBI and EMIR observations, the  $^{12}\text{CO}(7-6)$  spectrum is a combination of EMIR and SHFI data. The  $^{12}\text{CO}(1-0)$  line was measured by GBT and the  $^{12}\text{CO}(10-9)$  line by SMA, all other observations were taken with IRAM 30m and PdBI. The axes are flux (mJy) and frequency (GHz) (with the velocity shown on the upper horizontal axes) in all cases except for the average spectrum which has been plotted as km s $^{-1}$  and flux normalised to the peak value. Note that  $^{12}\text{CO}(7-6)$  and [C I](2–1) lines abut each other in the spectrum.

defined to include the mass of Helium such that  $M_{\text{H}_2} = M_{\text{gas}}$ ; see Solomon & Vanden Bout 2005 for a review).

There is considerable uncertainty about the correct value of  $\alpha$  to adopt in high-redshift galaxies (e.g. Baker et al. 2004; Coppin et al. 2007; Tacconi et al. 2008 and Ivison et al. 2010c) and similar uncertainty about the conversion factor to transform high- $J_{\text{upper}}$  CO transitions to the equivalent CO(1–0) fluxes (if required). However, we can estimate a minimum mass (and so a lower limit on  $\alpha$ ) assuming the  $^{12}\text{CO}(1-0)$  emission is optically thin (which is unlikely to be the case) and has solar abundance, following Ivison et al. (2010):

$$\frac{M(\text{H}_2)}{L'_{\text{CO}(1-0)}} \sim 0.08 \left( \frac{g_1}{Z} e^{-T_o/T_k} \left( \frac{J(T_k) - J(T_{\text{bg}})}{J(T_k)} \right) \right)^{-1} \times \left( \frac{[^{12}\text{CO}/\text{H}_2]}{10^{-4}} \right)^{-1} \frac{M_{\odot}}{\text{K km s}^{-1} \text{pc}^2}$$

where  $T_o = E_1/k_B \sim 5.5$  K,  $J(T) = T_o(e^{T_o/T} - 1)^{-1}$ ,  $T_{\text{bg}} = (1+z)T_{\text{CMB}} \sim 9.1$  K ( $T_{\text{CMB}} = 2.73$  K at  $z = 0$ ),  $z = 2.3259$ ,  $g_1 = 3$  (the degeneracy of level  $n = 1$ ),  $Z \sim 2(T_k/T_o)$  and  $[^{12}\text{CO}/\text{H}_2] \sim 10^{-4}$  for a solar metallicity environment (Bryant & Scoville 1996). For typical star-forming gas,  $T_k \sim 40$ –60 K, so to derive a minimum mass we use

$T_k = 40$  K. With  $L'_{12\text{CO}(1-0)} = 173 \pm 9 \times 10^8$  K km s $^{-1}$  pc $^2$ , this gives us a minimum gas mass of  $M_{\text{gas}} \gtrsim 1 \times 10^{10} M_{\odot}$  and a lower limit on  $\alpha \gtrsim 0.54$ .

We can then compare this to the dynamical mass adopting  $M_{\text{dyn}} = 5 R \sigma^2 / G$  (Solomon & Vanden Bout 2005). This assumes the dynamics of the CO emission trace the virialised potential well of the system and that the CO is distributed in a sphere of constant density with  $r \sim 1$  kpc (see §3.4 and Swinbank et al. 2010). Using the width of the  $^{12}\text{CO}(1-0)$  line,  $\sigma \sim 200$  km s $^{-1}$ , we estimate a dynamical mass of  $M_{\text{dyn}} \sim 5.3 \times 10^{10} M_{\odot}$ . If this mass is dominated by gas, then the upper limit on  $\alpha$  is  $\alpha = M_{\text{gas}}/L'_{12\text{CO}(1-0)} < 3$ .

Using this dynamical mass and the minimum gas mass, we place a lower limit on the gas fraction of  $M_{\text{gas}}/M_{\text{dyn}} \gtrsim 0.19$ . This ratio is similar to the ratio for typical starburst nuclei and the ratio of 30% found in M82 (Devereux et al. 1994). Compared to other high-redshift sub-millimetre galaxies (SMGs), using the  $^{12}\text{CO}(3-2)$  observations from Greve et al. (2005) and adopting  $\alpha = 0.8$  and  $R_{3,1} = 0.58 \pm 0.05$  from Ivison et al. (2010c), we find a median gas mass ratio of 50% for luminous SMGs, whilst Tacconi et al. (2008) derive a gas mass fraction of 0.3 for more typical star-forming galaxies at similar redshifts. We stress, however, that compared to the gas mass of  $6 \times 10^8 M_{\odot}$

within the central 1.2 kpc of M82 (Young & Scoville 1984), our gas mass is nearly two orders of magnitude higher, underlining the more extreme conditions in the central regions of SMM J2135.

In order to provide a simple comparison with previous studies, we estimate the gas mass of SMM J2135 using a conversion factor of  $\alpha \sim 0.8$  which applies to the smoothly distributed, high-pressure, largely molecular ISM measured in local ULIRGs (Downes & Solomon 1998; Solomon & Vanden Bout 2005, although recent local studies on high- $J_{\text{upper}}$  CO lines imply multi-phase ISM in ULIRGs as opposed to smoothly distributed) and is also the canonical value used for high-redshift LIRGs and ULIRGs (Tacconi et al. 2008; Stark et al. 2008). This value of  $\alpha$  is comfortably between the upper and lower limits calculated above. With this assumption the  $^{12}\text{CO}(1-0)$  line luminosity yields a total gas mass of  $M_{\text{H}_2} = (1.4 \pm 0.1) \times 10^{10} M_{\odot}$  (see also Swinbank et al. 2010).

Taking our estimate of the total gas mass and the expected size of  $\sim 1$  kpc for the system (Swinbank et al. 2010), we derive an average column density of  $\sim 10^{24} \text{ cm}^{-2}$ , which is comparable to the molecular hydrogen density in Arp 220, averaged over a similar region (Gerin & Phillips 1998), but much higher than the density in typical starburst galaxies such as M82. However, this estimate gives an average over the system which we know to be structured and so indicates that the column density is very high in parts of this source. The associated extinction is expected to exceed  $A_V \sim 10^3$ , suggesting significant absorption even in the far-infrared and moreover that the emission from some of the more common species we see is optically thick. With this extinction, coupled with our high value for  $G_0$  (derived in §3.2.1), high infrared luminosity and potentially high cosmic ray flux (see below), it is probable that momentum-driven outflows will result. These outflows could be either photon-driven (Thompson et al. 2005) or cosmic ray-driven (Socrates et al. 2008) and will impact both the dynamics of the gas in the system and the steady-state assumption in our PDR modelling (§3.2.1).

We can now compare the star-formation efficiency in SMM J2135 to that in the wider SMG and ULIRG populations. First we note that the far-infrared luminosity of SMM J2135 is  $L_{\text{FIR}} = (2.3 \pm 0.1) \times 10^{12} L_{\odot}$  (Ivison et al. 2010) which indicates a star formation rate (SFR) of  $\sim 400 \pm 20 M_{\odot} \text{ yr}^{-1}$  (Kennicutt 1998) assuming a Salpeter IMF. We combine the star-formation rate and gas mass to estimate the star formation efficiency (SFE) following Greve et al. (2005),  $\text{SFE} = L_{\text{FIR}}/M_{\text{H}_2}$  resulting in  $\text{SFE} \sim 165 \pm 7 L_{\odot} M_{\odot}^{-1}$ . This is comfortably within the limit derived by Scoville (2004) of  $[L_{\text{FIR}}/M_{\text{H}_2}]_{\text{max}} = 500 L_{\odot} M_{\odot}^{-1}$ , assuming Eddington-limited accretion of gas onto OB star clusters.  $^{12}\text{CO}(1-0)$  measurements in local ULIRGs derive a SFE of  $180 \pm 160 L_{\odot} M_{\odot}^{-1}$ , which is comparable to that in our source. The SFE of our source is also comparable to the median SFE of  $210 \pm 80 L_{\odot} M_{\odot}^{-1}$  for the sample of luminous SMGs of Greve et al. (2005), after correcting the latter using  $R_{3,1} = 0.58$  as appropriate for SMGs (Harris et al. 2010; Ivison et al. 2010c).

We begin modelling this system by noting that the 870- $\mu\text{m}$  SMA observations and comparison to the LABOCA flux reveal four bright, compact clumps embedded in a much more extended system with the clumps emitting  $\sim 80\%$  of

the total luminosity, and the rest of the emission emerging from a more extended component (Swinbank et al. 2010). Motivated by this structure we fit a two-component model to the dust SED, fixing the characteristic temperature of the cool (presumably more extended) component at 30 K and allowing the size and the characteristic temperature of the clumps to vary. The best fit yields a characteristic size for the clumps of  $r \sim 200$  pc at a temperature of  $T_{\text{d,warm}} = 57 \pm 3$  K, while the extended component has a size of  $r \sim 1000$  pc at  $T_{\text{d,cool}} = 30$  K. The dust mass of both the extended component and the clumps is then  $(1.5 \pm 0.2) \times 10^8 M_{\odot}$ , which is similar to the mass determined for the cool dust component in Ivison et al. (2010). The inferred clump size is somewhat larger than the size of the dust emission regions seen in the highest resolution 870- $\mu\text{m}$  SMA maps, where the clumps appear to be 100–200 pc in diameter (Swinbank et al. 2010). However, we note that forcing the clump sizes down to that size requires an increase in the characteristic temperature up to  $\sim 80$  K, and to keep the emission consistent with the integrated SED the clumps must then be optically thick at  $\sim 200 \mu\text{m}$  in the rest-frame. Clearly this two-component model is not a unique description of the dust emission from SMM J2135, but it does suggest that the system could be modelled by a combination of warm, compact and cooler, more extended dust component.

### 3.1.2 $^{12}\text{CO}$ SLED

To investigate the excitation within the ISM, we next construct the  $^{12}\text{CO}$  SLED by calculating the  $^{12}\text{CO}$  flux of each transition over the velocity range defined by the composite spectrum; we show the resulting SLED in Fig. 2. In Table 4 we also give the velocity-averaged brightness temperature ratios between  $^{12}\text{CO}(J_{\text{upper}})$  and  $^{12}\text{CO}(1-0)$ , which we define as  $R_{J,1} = L'(J+1 \rightarrow J)/L'(1 \rightarrow 0)$  (Greve et al. 2003; Harris et al. 2010). The  $^{12}\text{CO}$  SLED shows a continuous rise out to  $J_{\text{upper}} = 6$ , followed by a sharp decline as far as  $J_{\text{upper}} = 10$ . The brightness ratios of all of the  $J_{\text{upper}} > 2$  line luminosities compared to the  $^{12}\text{CO}(1-0)$  are  $< 1$ , which interpreted in the framework of a single phase ISM would indicate that the gas is sub-thermalised (the thermalised prediction is  $\sim 1$ ; Devereux et al. 1994). Indeed the  $L'_{12\text{CO}(3-2)}/L'_{12\text{CO}(1-0)}$  line luminosity ratio for SMM J2135,  $0.68 \pm 0.03$ , is similar to that seen in local starburst galaxies,  $0.64 \pm 0.06$  (Devereux et al. 1994). However, as Harris et al. (2010) discuss and as we show later in §3.2, these ratios are more likely to indicate a multi-phase ISM as found in star-forming regions locally.

The peak of the SLED at  $J_{\text{upper}} = 6$  is similar to that seen in nearby starburst galaxies such as NGC 253 and M82 (Bradford et al. 2003; Weiß et al. 2005; Panuzzo et al. 2010) and AGN, e.g. Mrk 231 (Papadopoulos et al. 2007; van der Werf et al. 2010). However, the overall shape of the SLED suggests that SMM J2135 has proportionally stronger  $^{12}\text{CO}(1-0)$  emission (compared to the higher  $J_{\text{upper}}$  transitions) than any of these galaxies, indicating the presence of an additional low-excitation gas phase. Nevertheless, the bulk of the cooling, 60%, arises through the  $^{12}\text{CO } J_{\text{upper}} = 5-7$  line emission, with a further 20% at  $^{12}\text{CO } J_{\text{upper}} \geq 8$ . van der Werf et al. (2010) have recently constrained the  $^{12}\text{CO}$  in Mrk 231 up to  $J_{\text{upper}} = 13$  with *Herschel*, building upon the earlier study of Papadopoulos et al. (2007), and

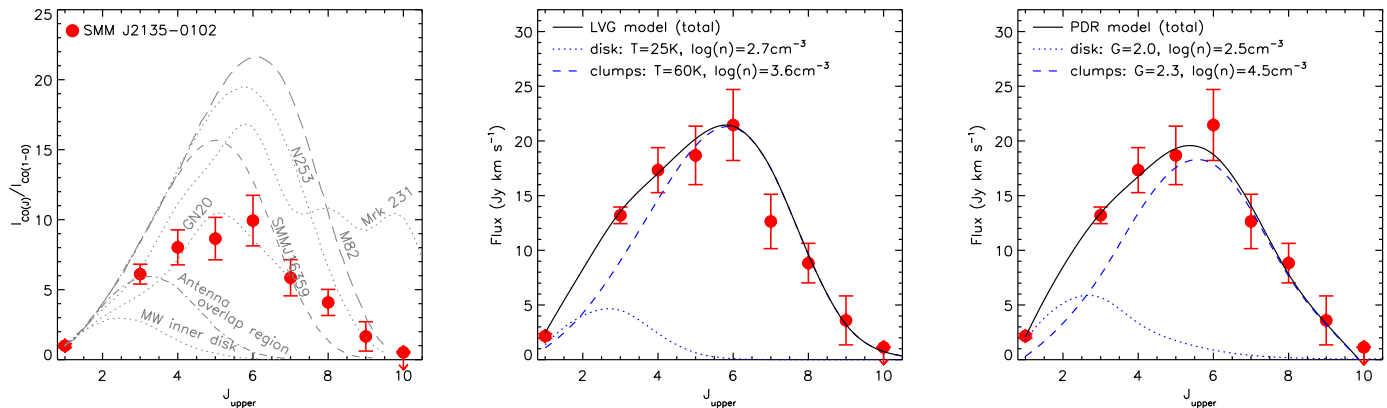


**Figure 2.** The integrated  $^{12}\text{CO}$  SLED for SMM J2135 showing that the SLED peaks around  $J_{\text{upper}} = 6$  (similar to M82, but with proportionally stronger  $^{12}\text{CO}(1-0)$ ). The central panel shows the results of LVG modelling applied to the integrated SLED, which requires two temperature phases to yield an adequate fit. In this model they have characteristic temperatures of  $T_{\text{kin}} = 25$  K and 60 K and densities of  $n = 10^{2.7}$  and  $10^{3.6} \text{ cm}^{-3}$  respectively (we associate these two phases with a cool, extended disk and hotter, more compact, clumps). The right-hand panel shows a similar comparison but now using a PDR model (Meijerink et al. 2007; see §3.2.1) which again requires a combination of both low- and high-density phases to adequately fit the integrated SLED.

show that, unlike nearby starbursts (e.g. NGC 253 or M 82), the  $^{12}\text{CO}$  line luminosity is roughly flat across  $J_{\text{upper}} = 5$ –13. They calculate that only 4% of the total  $^{12}\text{CO}$  line luminosity arises from the three lowest transitions, compared to  $\sim 20\%$  in the three lowest transitions of our  $^{12}\text{CO}$  SLED (and 43% in the Milky Way). The luminous high- $J_{\text{upper}}$  emission they see is likely due to the presence of additional excitation phases in Mrk 231, either high excitation PDRs or more likely an X-ray dominated region (XDR) (Spaans & Meijerink 2008). As we see later, we also find evidence for at least two phases of material in SMM J2135.

In comparison to higher-redshift sources, we see that the  $^{12}\text{CO}$  SLED for SMM J2135 has a broadly similar shape to that seen in other high-redshift SMGs, e.g. GN 20 (Carilli et al. 2010) or SMM J16359 (Weiß et al. 2005). Indeed, recent progress with EVLA and GBT has started to provide  $^{12}\text{CO}(1-0)$  detections of SMGs to complement the earlier  $^{12}\text{CO}(3-2)$  studies from PdBI (e.g. Greve et al. 2005). Using these two transitions, we find that the  $R_{3,1}$  brightness temperature ratio we derive for SMM J2135 (Table 4) is comparable to typical SMGs:  $R_{3,1} = 0.55 \pm 0.05$  (Ivison et al. 2010c) and  $R_{3,1} = 0.68 \pm 0.08$  (Harris et al. 2010), suggesting that the CO SLED results we derive for SMM J2135 may be applicable to the wider SMG population.

To investigate the excitation of the gas reservoir within this galaxy in more detail we exploit the fact that the shape of the  $^{12}\text{CO}$  SLED can provide information on the underlying gas density and temperature distributions and use a spherical large velocity gradient model (LVG; Weiß et al. 2005) to attempt to fit the observed SLED. LVG techniques are the most widely used radiative transfer model which can account for photon transport when spectral lines are optically thick, and can be used for efficiently solving the radiative transfer equation when the molecule level populations are not thermalised (Bayet et al. 2006).

Thus we next use the LVG code to model the  $^{12}\text{CO}$  SLED. The model assumes spherical symmetry and uniform kinetic temperature and density, a CMB background temperature of  $T_{\text{CMB}} = 2.73\text{K}(1+z)$  which at  $z = 2.3$  is  $\sim 9$  K,

the collision rates from Flower (2001) with an ortho/para  $\text{H}_2$  ratio of 3 and a ratio of the CO abundance to the velocity gradient of  $\text{CO}/dv/dr = 10^{-5} \text{ pc (km s}^{-1})^{-1}$ . To fit absolute line intensities the model further uses the source solid angle size,  $\Omega_S$ , which can be expressed in terms of the equivalent radius of a face-on disk,  $r_0 = D_A \sqrt{(\Omega_S/\pi)}$ . The model returns the temperature, density and size of the emission region.

Modelling the  $^{12}\text{CO}$  SLED in this way, we find that a single temperature and density phase is unable to fit the SLED, and that two or more phases are required. This is consistent with the implication of the model of the dust SED and the sub-millimetre morphology: we need at least two temperature phases to adequately describe this system. This need for multiple phases to fit the ISM in a high-redshift galaxy is unusual (however cf. Carilli et al. 2010), although it is not unexpected given that such multi-phase ISMs are commonly required in local galaxies (e.g. Wild et al. 1992; Guesten et al. 1993; Aalto et al. 1995; Mao et al. 2000; Ward et al. 2003). Thus, motivated by the fit to the dust SED we identify a two-phase fit to the SLED comprising four clumps and an extended phase, which provides an adequate fit (Fig. 2). In this model, the low-excitation phase peaks at  $J_{\text{upper}} \sim 3$  and is diffuse, with  $n \sim 10^{2.7} \text{ cm}^{-3}$  and  $T_{\text{kin}} \sim 25$  K. The denser, mildly-excited phase peaks around  $J_{\text{upper}} = 5$ –6, has  $T_{\text{kin}} \sim 60$  K and  $n \sim 10^{3.6} \text{ cm}^{-3}$  and contributes  $\sim 60\%$  of the total luminosity over all the  $^{12}\text{CO}$  lines (Fig. 2). The low-excitation phase has a  $^{12}\text{CO}$  SLED which is very similar to the inner disk of the Milky Way, while the warmer phase is well matched to the inner few hundred parsecs of the starburst region in NGC 253. Within this two phase model, the total gas mass is  $M_{\text{gas}} \sim (4.0 \pm 0.1) \times 10^{10} M_{\odot}$ , a factor of  $\sim 3\times$  the mass we determine from  $^{12}\text{CO}(1-0)$ , assuming  $\alpha = 0.8$ , corresponding to an effective  $\alpha = 2.0$  (similar to that derived for the nucleus of Arp 220; (Scoville et al. 1997)). From here on we adopt this value as the gas mass of our system, but note some of the differences if we had used the  $^{12}\text{CO}$  line luminosity and  $\alpha = 0.8$ , as is commonly assumed in



the analysis of high-redshift galaxies. The combination of this higher value for  $\alpha$  and our estimate of  $R_{3,1}$  would increase the gas mass by a factor of  $\sim 4\times$  over that estimated by assuming  $\alpha = 0.8$  and  $R_{3,1} = 1$  as usually assumed at high redshift (see also Ivison et al. 2010; Harris et al. 2010). Adopting  $\alpha \sim 2$  results in a gas mass fraction in the central 1kpc radius region of SMM J2135 of 75% (and closer to the 100% for typical SMGs, Greve et al. 2005) subject to uncertainties on the dynamical mass due to the unknown configuration of the gas within the system.

### 3.1.3 Atomic Carbon

We have also obtained strong detections of the  $[\text{C I}](^3\text{P}_1 \rightarrow ^3\text{P}_0)$  and  $[\text{C I}](^3\text{P}_2 \rightarrow ^3\text{P}_1)$  emission lines, and from these we can begin to investigate the properties of the ISM. We start by noting the similar detailed morphologies of the  $[\text{C I}](^3\text{P}_1 \rightarrow ^3\text{P}_0)$  and the  $^{12}\text{CO}(3-2)$  and  $^{12}\text{CO}(1-0)$  lines in Fig. 1, which suggests that the emission is arising from the same mix of phases with characteristic temperatures of  $T \lesssim 40$  K. Indeed observations of neutral carbon transitions have shown that the ratio of  $L'_{[\text{C I}](^3\text{P}_2 \rightarrow ^3\text{P}_1)} / L'_{[\text{C I}](^3\text{P}_1 \rightarrow ^3\text{P}_0)}$  provides a sensitive probe of the temperature of the interstellar medium at moderate densities. Both lines have modest critical densities ( $n_{\text{crit}} \sim 0.3\text{--}1.1 \times 10^3 \text{ cm}^{-3}$ ) and are therefore often thermalised in molecular clouds with  $n \gtrsim 10^3 \text{ cm}^{-3}$ . The lines arise from states with energy levels  $T_1 = 23.6$  K and  $T_2 = 62.5$  K above the ground state, and thus their ratio is sensitive to the gas temperature if  $T_{\text{gas}} \lesssim 100$  K. We derive  $L'_{[\text{C I}](^3\text{P}_2 \rightarrow ^3\text{P}_1)} / L'_{[\text{C I}](^3\text{P}_1 \rightarrow ^3\text{P}_0)} = 0.37 \pm 0.02$ , which is similar to that measured in nearby starbursts and galactic nuclei such as M 82 and NGC 253 where  $L'_{[\text{C I}](^3\text{P}_2 \rightarrow ^3\text{P}_1)} / L'_{[\text{C I}](^3\text{P}_1 \rightarrow ^3\text{P}_0)} \sim 0.33$  (Bennett et al. 1994; White et al. 1994; Israel et al. 1995; Bayet et al. 2004), but larger than typically found in the cooler, dense cores of giant molecular clouds (e.g. Zmuidzinas et al. 1988). To be compatible with previous studies we define  $R_{[\text{C I}]}$  as the ratio of the  $[\text{C I}](^3\text{P}_2 \rightarrow ^3\text{P}_1)$  to  $[\text{C I}](^3\text{P}_1 \rightarrow ^3\text{P}_0)$  temperature integrated line intensities in  $\text{K km s}^{-1}$ . In SMM J2135 we derive an integrated line ratio of  $R_{[\text{C I}]} = 0.88 \pm 0.01$ . We can use this ratio to estimate the excitation temperature  $T_{\text{ex}}$  following Stutzki et al. (1997),  $T_{\text{ex}} = 38.8 \text{ K} / \ln(2.11/R_{[\text{C I}]})$ , and derive  $T_{\text{ex}} = 44.3 \pm 1.0$  K for SMM J2135.

We also follow Weiß et al. (2005) to derive the total mass of neutral carbon via:

$$M_{\text{C I}} = 1.902 \times 10^{-4} Q(T_{\text{ex}}) e^{T_1/T_{\text{ex}}} L'_{[\text{C I}](^3\text{P}_1 \rightarrow ^3\text{P}_0)} \quad (1)$$

where  $Q(T_{\text{ex}}) = 1 + 3e^{-T_1/T_{\text{ex}}} + 5e^{-T_2/T_{\text{ex}}}$  is the  $[\text{C I}]$  partition function and  $T_{\text{ex}}$  is defined above. Using  $T_{\text{ex}} = 44.3 \pm 1.0$  K and our measured luminosity of the upper fine structure line,  $[\text{C I}](^3\text{P}_1 \rightarrow ^3\text{P}_0)$ , we estimate a carbon mass of  $M_{[\text{C I}]} = (9.1 \pm 0.2) \times 10^6 M_{\odot}$ . Combining this with our gas mass estimated from the LVG analysis we derive a  $[\text{C I}]$  abundance of  $M([\text{C I}])/6M(\text{H}_2) = (3.8 \pm 0.1) \times 10^{-5}$ , which is higher than the Galactic value of  $2.2 \times 10^{-5}$  from Frerking et al. (1989). Similarly, the ratio of the  $[\text{C I}]$  and  $^{12}\text{CO}$  brightness temperatures,  $L'_{[\text{C I}](^3\text{P}_1 \rightarrow ^3\text{P}_0)} / L'_{^{12}\text{CO}(1-0)} = 0.41 \pm 0.02$ , falls towards the upper end of the range  $0.2 \pm 0.2$  observed in local galaxies (Gerin & Phillips 2000; Bayet et al. 2006). A higher abundance of  $[\text{C I}]$  relative to  $^{12}\text{CO}$  is expected in regions with lower metallicity (Stark et al. 1997) where  $^{12}\text{CO}$  is photo-

dissociated, in regions with a high ionisation fraction which may drive the chemistry to equilibrium at a high  $[\text{C I}]/^{12}\text{CO}$  ratio, and in starburst systems with a high cosmic ray flux (Papadopoulos et al. 2004; Flower et al. 1994).

We can also attempt to model the  $[\text{C I}]$  emission within the framework of our two-phase LVG model. We find that we are only able to simultaneously fit the  $[\text{C I}]$  luminosities and ratios if the carbon abundance is allowed to vary between the two phases. To fit the observed  $R_{[\text{C I}]}$  ratio and the  $[\text{C I}]$  to  $^{12}\text{CO}$  brightness temperatures the LVG model suggests  $[\text{C I}]/^{12}\text{CO} \sim 0.2$  for the warm, dense phase, which is close to the Galactic value,  $[\text{C I}]/^{12}\text{CO} \sim 0.13$  (Frerking et al. 1989), while for the extended, low-density phase we require an abundance of  $[\text{C I}]/^{12}\text{CO} \sim 3.0$ , which suggests a deficit of oxygen, and hence possibly a very low metallicity. Using the correlation between  $[\text{C I}]/^{12}\text{CO}$  and metallicity ( $12 + \log(\text{O}/\text{H})$ ) in Bolatto et al. (2000), for the cool component we derive  $12 + \log(\text{O}/\text{H}) = 7.5$  and hence a metallicity of  $\sim Z/Z_{\odot} = 1/25$ . This is similar to that of the Sextans dwarf galaxy, to the lowest metallicity, young starbursts seen locally (Brown et al. 2008), and to the lowest metallicity galaxies found at high redshift (Yuan & Kewley 2009). However, the high  $[\text{C I}]/^{12}\text{CO}$  ratio could also be due to a high cosmic ray flux in the galaxy (Papadopoulos et al. 2004; Israel & Baas 2002). Indeed a factor of  $\sim 10\times$  enhancement of cosmic ray flux will yield the high  $[\text{C I}]/^{12}\text{CO}$  ratio we observe and this may not be unlikely given the high star formation rate density of the star-forming regions (Swinbank et al. 2010). Moreover, an enhanced  $[\text{C I}]/^{12}\text{CO}$  ratio has also been observed in the starburst galaxy NGC 253 (Harrison et al. 1995; Bradford et al. 2003) attributed to a high cosmic ray flux.

Finally, the  $[\text{C I}]$  detections can be combined with the observations of  $[\text{C II}]\lambda 157.7$  from Ivison et al. (2010) to investigate the ISM cooling. We can compare the cooling in each of our lines relative to the bolometric ( $8\text{--}1000\mu\text{m}$ ) luminosity, to assess their importance. The fraction of the bolometric luminosity in the  $[\text{C II}]$  line is 0.24%, the rotational  $^{12}\text{CO}$  lines ( $^{12}\text{CO}(1-0)$  to  $^{12}\text{CO}(10-9)$ ) contribute 0.09% and the  $[\text{C I}]$  lines result in just 0.03%. Therefore,  $[\text{C II}]$  dominates the cooling with the total cooling due to  $^{12}\text{CO}$  and  $[\text{C I}]$  representing  $\sim 50\%$  of the cooling due to  $[\text{C II}]$ .  $[\text{C II}]$  is one of the brightest emission lines in galaxies and can account for 0.1–1% of the far-infrared luminosity of the nuclear regions of galaxies (Stacey et al. 1991); our source lies well within that range. This situation is in contrast to comparably luminous systems in the local Universe, e.g. Arp 220, where the  $[\text{C II}]$  emission is just  $1.3 \times 10^{-4}$  of  $L_{\text{FIR}}$  (Gerin & Phillips 1998). This most likely results from saturation of  $[\text{C II}]$  in very high-density star-forming regions (Luhman et al. 1998). The proportionally stronger  $[\text{C II}]$  emission we see in SMM J2135 may then reflect slightly lower densities and more extended star formation (Ivison et al. 2010c), or be due to the lower metallicity of the gas compared to local ULIRGs (Israel et al. 1996; Maiolino et al. 2009).

Overall, our observations of atomic carbon suggest that it arises from a cool phase within the galaxy and that integrated over the whole galaxy the  $[\text{C I}]/^{12}\text{CO}$  ratio is higher than the Galactic value. However, we also find evidence for variation in the ratio within the system, with the cool, low-density phase having significantly enhanced  $[\text{C I}]$ , compared



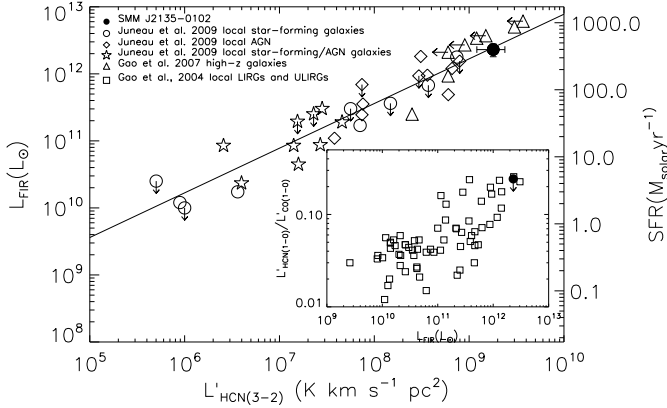


**Figure 3.** The relation between far-infrared luminosity and HCN luminosity for galaxies. We compare our observations of SMM J2135 with the correlation seen locally and find that this high-redshift galaxy follows the tight correlation seen in local galaxies (Juneau et al. 2009). In the main panel we plot observations from a sample of 34 local galaxies (star-forming galaxies, star-forming galaxies with AGN and strong AGN) taken from Juneau et al. (2009). In the inset panel we compare our upper limit on the ratio of  $L'_{\text{HCN}(1-0)} / L'_{\text{CO}(1-0)}$  to the ratio in local LIRGs and ULIRGs from Gao & Solomon (2004) showing that this upper limit is consistent with the Gao & Solomon (2004) relation. Again we see that the properties of the dense gas and far-infrared emission in this galaxy are similar to those seen locally.

to  $^{12}\text{CO}$ , suggesting lower metallicity in this phase or a higher cosmic ray flux in the overall system.

### 3.1.4 HCN(3-2)

Our spectra also cover emission lines from a number of species other than  $^{12}\text{CO}$ ; notably, we detect HCN(3-2) emission (Table 2). HCN is an effective tracer of dense gas due to its high dipole moment, requiring  $\sim 100\times$  higher densities for collisional excitation than  $^{12}\text{CO}(1-0)$ . Indeed, HCN is one of the most abundant molecules at densities  $n \gtrsim 3 \times 10^4 \text{ cm}^{-3}$  (compared to critical densities of  $\gtrsim 500 \text{ cm}^{-3}$  for low- $J_{\text{upper}}$  levels of  $^{12}\text{CO}$ ). We note that the velocity centroid of the HCN emission is redshifted by approximately  $+230 \pm 100 \text{ km s}^{-1}$ , relative to the nominal systemic redshift of the system derived from  $^{12}\text{CO}$ . As we discuss below, this hints that the HCN emission may arise predominantly from only one of the kinematic components within the galaxy.

It has been shown that the HCN line luminosity is tightly correlated with far-infrared luminosity in local spirals and ULIRGs, with a linear relation holding over at least three decades in luminosity, and a similar relation may hold at high redshift (Fig. 3; Gao & Solomon 2004; Gao et al. 2007). This suggests that HCN is a good tracer of the dense gas which fuels the massive star formation, which in turn is responsible for the far-infrared emission. In Fig. 3 we show the relation between far-infrared luminosity and HCN(3-2) line luminosity for local spirals, LIRGs and ULIRGs (Gao & Solomon 2004; Juneau et al. 2009). SMM J2135 lies at the high-luminosity end of this

correlation, corresponding to the highest-luminosity local ULIRGs, and is consistent with the relation. In the inset panel on Fig. 3 we also compare our source to local LIRGs and ULIRGs in Gao & Solomon (2004). We show the upper limit on  $L'_{\text{HCN}(1-0)} / L'_{\text{CO}(1-0)}$  using our  $3\text{-}\sigma$  upper limit for HCN(1-0) flux, demonstrating that this is also consistent with the increasing  $L'_{\text{HCN}} / L'_{\text{CO}}$  ratio seen with increasing  $L_{\text{FIR}}$  at low redshift.

It is also possible to estimate a total gas mass from the HCN luminosity (Gao et al. 2005). Using our  $3\text{-}\sigma$  upper limit on the HCN(1-0) luminosity we derive a limit on the dense gas mass of  $M_{\text{dense}}(\text{H}_2) = \alpha_{\text{HCN}(1-0)} L'_{\text{HCN}} \ll 4.5 \times 10^{10} M_{\odot}$  with  $\alpha_{\text{HCN}} \ll 10$  (Gao & Solomon 2004). We caution that there is at least a factor  $3\times$  uncertainty arising from the uncertainty in  $\alpha_{\text{HCN}}$ . The value of  $\alpha_{\text{HCN}}$  we adopt is appropriate for a virialised cloud core; however, ULIRGs and LIRGs usually have a much higher HCN brightness temperature, resulting in their  $\alpha_{\text{HCN}}$  being much lower (Gao & Solomon 2004), and hence this is reported as an upper limit on the gas mass. Since this gas mass is consistent with the mass derived from our LVG analysis of  $^{12}\text{CO}$ , this suggests that with better estimates of  $\alpha_{\text{HCN}}$ , HCN may be a promising route to constraining the dense gas masses of high-redshift galaxies in the future. However, we note that the consistency of  $^{12}\text{CO}$ -based and HCN-based gas mass estimates may be coincidental if these lines trace different phases. We further caution that at least two HCN lines may be required to derive the correct value of  $\alpha_{\text{HCN}}$  due to the strong variations in HCN(4-3)/HCN(1-0) and HCN(3-2)/HCN(1-0) luminosity ratios locally (Papadopoulos 2007).

As with [C], we also attempted to use our two-phase LVG model from the  $^{12}\text{CO}$  SLED to model the HCN(3-2) and HCN(1-0) emission from this system. However, we find that any models which fit the HCN SLED, in particular the bright HCN(3-2) emission, over-predict the luminosities of the  $^{12}\text{CO}$  SLED and result in gas masses which are greater than the dynamical mass. A similar problem has been identified in local ULIRGs which exhibit enhanced HCN line emission and high ratios of  $L'_{\text{HCN}} / L'_{\text{CO}}$  due to a higher proportion of dense gas in these strong starburst systems (Solomon & Vanden Bout 2005; Gao et al. 2007).

### 3.1.5 H<sub>2</sub>O

Finally we comment on the limits obtained for H<sub>2</sub>O. H<sub>2</sub>O emission arises from the warm, dense gas in the densest regions of a starburst or around an AGN. The strength of the emission is thus a probe of the radiation density and so reflects the compactness of the far-infrared source. The H<sub>2</sub>O(2<sub>1,1</sub>-2<sub>0,2</sub>) (731.681 GHz) emission line has recently been detected in the local ULIRGs Mrk 231 and Arp 220 (e.g. González-Alfonso et al. 2010) revealing warm, dense material, possibly arising from an XDR associated with AGN activity (see also Spaans & Meijerink 2008 and van der Werf et al. 2010). We compare our limits on the H<sub>2</sub>O line luminosities (as a fraction of bolometric luminosity) with Mrk 231 and Arp 220, where the luminosity ratios are  $L_{\text{H}_2\text{O}} / L_{\text{FIR}} \sim 1\text{--}2 \times 10^{-6}$ . We derive limits on the line luminosity ratio of  $L_{\text{H}_2\text{O}} / L_{\text{FIR}} < 1\text{--}5 \times 10^{-6}$  from the H<sub>2</sub>O(5<sub>1,5</sub>-4<sub>2,2</sub>) and H<sub>2</sub>O(2<sub>1,1</sub>-2<sub>0,2</sub>) transitions. These suggest that if an XDR exists within SMM J2135 it is unlikely to be more luminous than those seen in these local AGN-

dominated ULIRGs. This conclusion is reinforced by the relatively low luminosity of the high- $J_{\text{upper}}$   $^{12}\text{CO}$  lines in SMM J2135 compared to the substantially brighter high- $J$  lines in Arp 220 and Mrk 231 which again require an XDR to fit their  $^{12}\text{CO}$  SLEDs (Spaans & Meijerink 2008; van der Werf et al. 2010).

### 3.2 Integrated Properties: Physical Properties of the ISM

When massive stars are formed around a molecular cloud, their ultra-violet (UV) radiation changes the chemical properties of the cloud’s surface layers; the far-UV flux photodissociates the outer layer and ionises the material (such as carbon). This layer then cools primarily via atomic fine structure lines of [OI], [CII], [CI], and the rotational  $^{12}\text{CO}$  lines. Emission from these different coolants arises from different depths within the PDR (Kramer et al. 2004), such that the surface layers are dominated by emission from hydrogen, [CII] and oxygen, although further into the star-forming clouds (as the extinction,  $A_V$ , increases), hydrogen becomes molecular, whilst the ionisation of carbon declines, with [CII] becoming [CI] and then combining into CO. Moreover, with increasing density, the higher- $J_{\text{upper}}$   $^{12}\text{CO}$  emission becomes stronger, as do other molecular gas tracers such as HCN, CS and CN (Kaufman et al. 1999). Deeper into the cloud, the gas is molecular, but still has a higher temperature than in the far-UV shielded core. Significant effort has been devoted to modelling (and predicting) the fine structure and molecular emission line ratios associated with these star-forming regions using PDR models. These account for variations in density, temperature, clumpiness and time-dependent chemistry (e.g. Meijerink et al. 2007; Kaufman et al. 1999) and using their predictions of the ratios of [CII], [CI] and  $^{12}\text{CO}$  we can investigate the typical far-UV intensity and ISM density within the star-forming regions in SMM J2135.

#### 3.2.1 PDR models

To model the full-range of observed line ratios from SMM J2135 we use the PDR models of Kaufman et al. (1999) and Meijerink et al. (2007) in which the emission is determined by the atomic gas density ( $n$ ; the density of H nuclei) and the incident far-UV radiation field from massive stars ( $h\nu = 6\text{--}13.6\text{ eV}$ ) which is expressed in terms of  $G_0$  (where  $G_0$  is the average far-UV radiation field in the Milky Way and is expressed in Habing units:  $1.6 \times 10^{-3}\text{ erg s}^{-1}\text{ cm}^{-2}$ ). Simple PDR models (including one of the two models we compare to; Kaufman et al. 1999) calculate the line emission generated by a cloud illuminated only on one side. However, for observations of external galaxies it is not clear that such a “single cloud” model will adequately describe the observed molecular lines. For clouds illuminated on all sides we note that an observer will detect optically thin radiation emitted from both the near and far sides of the cloud, but only see optically thick emission from the near side. Generally, low- $J_{\text{upper}}$   $^{12}\text{CO}$  transitions are assumed to be optically thick for the nominal  $A_V = 10$  cloud depths in the PDR models (Hailey-Dunsheath et al. 2010b), whilst [CII], [CI],  $^{13}\text{CO}$  and  $L_{\text{FIR}}$  are assumed to

be optically thin (although note our earlier estimates of the high column densities and extinction in this system). We have not applied any corrections to the emission lines to account for these differences between optically thick and optically thin emission. Instead, we also compare to more complicated models involving two or more clouds, with differing densities and incident radiation fields which have been constructed by Meijerink et al. (2007). The implementation of these models assumes all emission lines are coming from the same gas in the same region, which we know to be a vast over-simplification; however, these solutions do provide us with order of magnitude estimates of the characteristic conditions in the system.

In Fig. 4 we show the model grid of  $n$  and  $G_0$  values for various emission line ratios for SMM J2135. The  $^{12}\text{CO } J/(J-1)$  and [CI]/ $^{12}\text{CO}$  line luminosity ratios vary over six orders of magnitude in  $G_0$ ; however, the [CII]/FIR and [CII]/ $^{12}\text{CO}$  ratios appear to break this degeneracy. Indeed, in the  $n \sim 10^3\text{--}10^5\text{ cm}^{-3}$  regime, these provide a strong constraint on  $G_0$ . Using the two different PDR models we convert the allowed parameter space for each line ratio to derive the peak likelihood solution, which is shown in Fig. 4 for both models. We find that the solutions cluster around moderate densities ( $n \sim 10^4\text{ cm}^{-2}$ ), similar to those claimed for local ULIRGs from PDR modelling of  $\text{H}_2$  emission (Davies et al. 2003). The peak likelihood solutions use all the line ratios available aside from the  $L'_{\text{[CI]}(3\text{P}_2 \rightarrow 3\text{P}_1)}/L'_{\text{[CI]}(3\text{P}_1 \rightarrow 3\text{P}_0)}$  ratio. This line’s track deviates strongly from the preferred solution from the other lines. We expect this reflects the sensitivity of this line ratio to details of the PDR, such as geometry, and we discuss specific problems with the PDR model treatment of [CI] below.

The best-fit solution to our suite of line ratios is  $n = 10^{4.1 \pm 0.3}\text{ cm}^{-3}$  and  $G_0 = 10^{3.6 \pm 0.7}$  Habing fields for the PDR models from Kaufman et al. (1999) and  $n \sim 10^{4.3 \pm 0.2}\text{ cm}^{-3}$  and  $G_0 \sim 10^{3.3 \pm 0.2}$  Habing fields from Meijerink et al. (2007). The best-fit solutions are within  $1\text{--}\sigma$  and are in agreement with earlier estimates based on just  $^{12}\text{CO}(1\text{--}0)$ , [CII] and  $L_{\text{FIR}}$  in Ivison et al. (2010). As we see from Fig. 4, these physical conditions are similar to local starburst galaxies and ULIRGs (Stacey et al. 1991; Davies et al. 2003) and at the upper end of both density and  $G_0$  for normal star-forming galaxies (Malhotra et al. 2001), for example the radiation field is  $\sim 1000\times$  more intense than in the disk of the Milky Way. The characteristic density compares well to the dense star-forming cores of Galactic molecular clouds, or to the central compact nuclear gas disks of local ULIRGs such as Arp 220 (Downes & Solomon 1998; Sakamoto et al. 1999) and is also consistent with the integrated  $^{12}\text{CO}$  SLED (see §3.1.2). This characteristic density we derive is greater than the critical density for [CII], [CI] and  $\text{CO}(1\text{--}0)$ , above which the intensity of the lines saturates. Similarly, the  $G_0$  value we derive suggests the conditions in the PDRs are at the limit of the steady state solution (Kaufman et al. 1999); with radiation pressure on grains comparable to turbulence, suggesting that the PDRs may be ionising material.

Our results imply that the underlying physics of the star formation occurring in the system is similar to the dense star-forming cores of Galactic molecular clouds (characteristic of massive OB star-forming regions), even though the total energetics of the system is far more extreme than in the disk of our galaxy. Interestingly, Teyssier et al. (2010) have

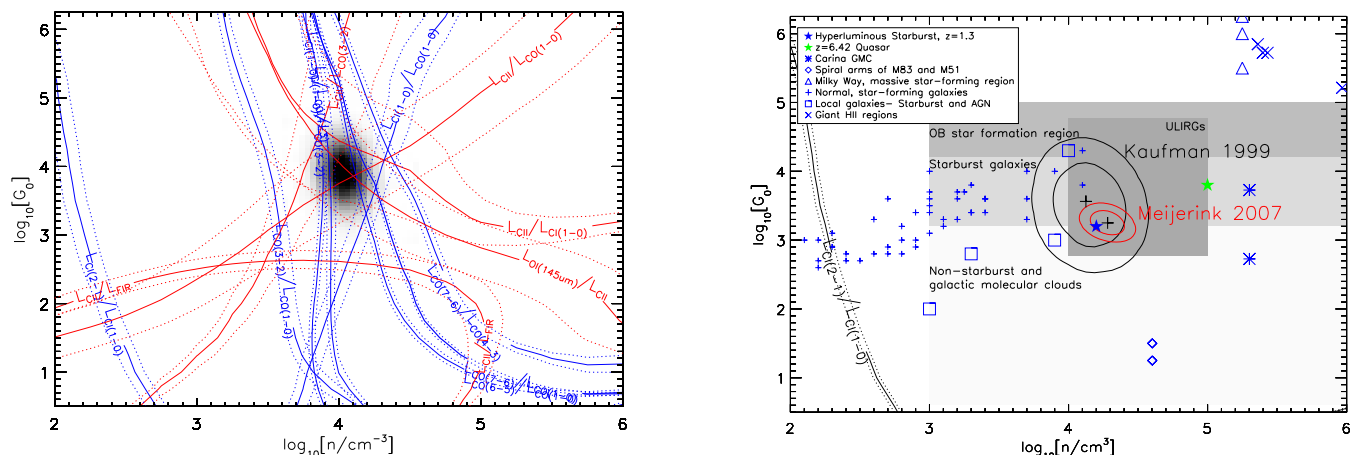


**Figure 4.** *Left:* Luminosity line ratios (in units of  $L_{\odot}$ ) from  $^{12}\text{CO}$ ,  $[\text{CI}]$  and  $[\text{CII}]$  as a function of density and far-UV flux ( $G_0$  in units of Habing field), from the PDR models of Kaufman et al. (1999). Tracks are drawn for the measured ratios in solid lines with the  $1\text{-}\sigma$  errors as dotted lines. The line ratios within SMM J2135 intercept at  $n \sim 10^{4.1} \text{ cm}^{-3}$  and  $G_0 \sim 10^{3.6}$  Habing fields and  $n \sim 10^{4.3} \text{ cm}^{-3}$  and  $G_0 \sim 10^{3.3}$  Habing fields for the Kaufman et al. (1999) and Meijerink et al. (2007) models respectively. To better display the preferred regions of parameter space we combine the probability distributions from all of these lines (excluding  $L_{[\text{CII}](2-1)}/L_{[\text{CII}](1-0)}$  for reasons explained in § 3.2) to derive a peak likelihood solution for each model. *Right:* The same parameter space for the models, now comparing the peak likelihood solutions from the model grids to the derived values of  $G_0$  and density ( $n$ ) for various low- and high-redshift galaxies and molecular clouds. We also indicate the regions of parameter space which are typically encompassed by Galactic OB star-formation regions, starburst galaxies and non-starburst and Galactic molecular clouds from Stacey et al. (1991). This shows that the line ratios for SMM J2135 are consistent with those typically found in local starbursts or ULIRGs. The local galaxy that lies within the contours of the peak likelihood for the Kaufman models is NGC 253, a spiral starburst galaxy (Negishi et al. 2001). We also show the peak likelihood solution derived from the PDR models of Meijerink et al. (2007) which provide a concomitant solution. The contours represent the  $1\text{-}$  and  $2\text{-}\sigma$  limits compared to the best-fit solution. The peak likelihood solutions are derived without including the  $L_{[\text{CII}](2-1)}/L_{[\text{CII}](1-0)}$  track, which we plot on both panels to show its discrepancy from the general solution from the other lines (see § 3.2).

recently used hydrodynamic simulations of major mergers of disk galaxies to show that the density of gas at which a majority of the star formation in these systems occurs is  $n \sim 10^4 \text{ cm}^{-3}$ , as we find here.

Of all the line ratios we analyse, the most obvious outlier in the PDR modelling is the  $[\text{C I}]({}^3P_2 \rightarrow {}^3P_1)/[\text{C I}]({}^3P_1 \rightarrow {}^3P_0)$  emission line ratio (Fig. 4). However, we note that this line ratio is one of the most sensitive to  $G_0$  and  $n$  and it would only require a modest increase in the predicted  $[\text{C I}]({}^3P_1 \rightarrow {}^3P_0)$  flux in the models,  $\sim 3\times$  stronger, to shift this track into agreement with the solution based on the bulk of the other ratios at  $n \sim 10^4 \text{ cm}^{-3}$  and  $G_0 \sim 10^{3.5}$ . This problem may arise because the PDR models assume a particular geometry, which determines the ratio of diffuse to dense gas, and assume a homogeneous medium (an unrealistic assumption for our source). The resulting luminosity ratios based on  ${}^{12}\text{CO}/[\text{C I}]$  and  $[\text{C I}]$  are sensitive to this geometry and the  $[\text{C I}]({}^3P_2 \rightarrow {}^3P_1)/[\text{C I}]({}^3P_1 \rightarrow {}^3P_0)$  ratio is particularly sensitive to the homogeneity of the medium (Spaans 1996), as demonstrated by the difficulty the models have in reproducing the  $[\text{C I}]({}^3P_1 \rightarrow {}^3P_0)$  or  $[\text{C I}]({}^3P_2 \rightarrow {}^3P_1)$  emission lines even in tranquil environments (e.g. Pineda & Bensc 2007; Papadopoulos & Greve 2004). Indeed, Papadopoulos & Greve (2004) argue that  $[\text{C I}]$  is distributed relatively ubiquitously in molecular clouds (the critical density for excitation of both  $[\text{C I}]({}^3P_1 \rightarrow {}^3P_0)$  and  $[\text{C I}]({}^3P_2 \rightarrow {}^3P_1)$  is roughly that of  ${}^{12}\text{CO}(1-0)$ ; Solomon & Vanden Bout 2005). This is contrary to PDR theory, which places  $[\text{C I}]$  in a narrow  $[\text{C II}]/[\text{C I}]/{}^{12}\text{CO}$  tran-

sition zone on the surface of far-UV illuminated molecular clouds, and potentially makes [C I] a very effective tracer of H<sub>2</sub> mass. Therefore our low ratio may be arising from geometrical optical depth effects in which the [C I] effectively follows the volume (rather than the PDR surface), which would naturally lower the  $[C I](^3P_2 \rightarrow ^3P_1) / [C I](^3P_1 \rightarrow ^3P_0)$  ratio (e.g. see Kramer et al. 2008) as would happen from any process which enhances [C I] emission through the cloud’s volume (e.g. cosmic rays). We also caution that the  $[C I](^3P_2 \rightarrow ^3P_1) / [C I](^3P_1 \rightarrow ^3P_0)$  ratio has been measured in only a few local galaxies (e.g. Bayet et al. 2006) and so the fine structure excitation of neutral carbon has yet to be fully characterised and calibrated locally.

### 3.2.2 Limits on $^{13}\text{CO}$ , CN, HNC and $\text{HCO}^+$

Our observations have also simultaneously covered a number of dense gas tracers and from these we can place limits on the line luminosities of  $^{13}\text{CO}$ , CN, HNC and  $\text{HCO}^+$ . We can then ask if these limits are consistent with our preferred characteristic density and UV radiation field from the PDR model.

First we consider the limits on the  $^{13}\text{CO}$ . The  $^{13}\text{C}$  nuclei are synthesised by CNO processing of  $^{12}\text{C}$  nuclei from earlier stellar generations ( $^{12}\text{C}$  is produced from He burning on rapid timescales in massive stars). Since  $^{13}\text{C}$  is produced more slowly in intermediate mass stars during the red giant phase (at  $\sim 1$  Gyr), the  $^{12}\text{C}/^{13}\text{C}$  ratio has been

TABLE 3.  
MODEL KINEMATIC PARAMETERS

Component	$v$ (km s <sup>-1</sup> )	$\sigma$ (km s <sup>-1</sup> )
Z <sub>2</sub>	-167 ± 9	75 ± 8
Z <sub>1</sub>	28 ± 9	75 ± 8
Y	165 ± 13	157 ± 17
X	396 ± 9	76 ± 9

Notes: Velocities and line widths of the three kinematic components seen in the CO and [C I] spectra. The velocities are given with respect to a heliocentric redshift of  $z = 2.32591$ .

proposed as a diagnostic of the nucleosynthesis history in galaxies. A high ratio would then be seen at high redshift as the young starbursts will have had insufficient time to form secondary nuclei of <sup>13</sup>CO. In the Milky Way and nearby star-forming galaxies, the <sup>12</sup>CO/<sup>13</sup>CO line luminosity ratio ( $L'_{12\text{CO}}/L'_{13\text{CO}}$ ) is  $\sim 5$ –10. However, local ULIRGs have shown a deficiency of <sup>13</sup>CO (possibly due to gas inflow; Rupke et al. 2008), which raises the <sup>12</sup>CO/<sup>13</sup>CO line ratio to  $\sim 30$  (Greve et al. 2009). Indeed, recently, Henkel et al. (2010) showed that the <sup>12</sup>CO/<sup>13</sup>CO luminosity line ratio in the Cloverleaf quasar ( $z=2.6$ ) is  $L'_{12\text{CO}}/L'_{13\text{CO}}=40\pm 17$ , suggestive of a deficiency of <sup>13</sup>CO. Within SMM J2135, we estimate limits on the ratio of  $>5.8$  and  $>6.5$  for the  $J_{\text{upper}}=1$  and  $J_{\text{upper}}=3$  transitions respectively. These limits are consistent with the Milky Way, but more sensitive observations are required to place firm conclusions as to whether a deficiency exists similar to that observed in other local ULIRGs and high-redshift galaxies.

We can compare these limits to the predictions from the PDR models of Meijerink et al. (2007). The model predictions are  $L'_{12\text{CO}}/L'_{13\text{CO}}=2.13$  and 2.08 for the  $J_{\text{upper}}=1$  and  $J_{\text{upper}}=3$  transitions respectively, indicating lower <sup>13</sup>CO abundance in SMM J2135-0102 than the model predicts. This may arise due to a number of effects. It is known that the line luminosity ratios of giant molecular clouds are lower than galaxy-integrated properties due to the lower opacity of <sup>13</sup>CO compared to <sup>12</sup>CO in the inter-cloud medium. Since we are measuring galaxy integrated properties, this would naturally lower the ratio. Clearly it would be useful to obtain a more sensitive observation of the <sup>13</sup>CO to determine the extent of this discrepancy with PDRs.

Finally, we note that the line luminosity ratio of the dense gas tracers of  $\text{CS}(2-1)/^{12}\text{CO}(1-0)<0.13$  is lower than that predicted from the PDR model (0.43). In contrast, the  $\text{HNC}(3-2)/^{12}\text{CO}(1-0)<1.3$  and  $\text{HCO}^+(3-2)/^{12}\text{CO}(1-0)<1.2$  are consistent with those predicted by the PDR models (1.3 and 0.15 respectively). A more detailed test of the model prediction for these dense gas tracers will again require more sensitive observations.

### 3.3 Kinematically Resolved Properties: Decomposed <sup>12</sup>CO SLED

With the high signal-to-noise of our observations of <sup>12</sup>CO and [C I] in Fig. 1, it is obvious that the spectra show significant kinematic structure and that more intriguingly this structure appears to vary between the different transitions

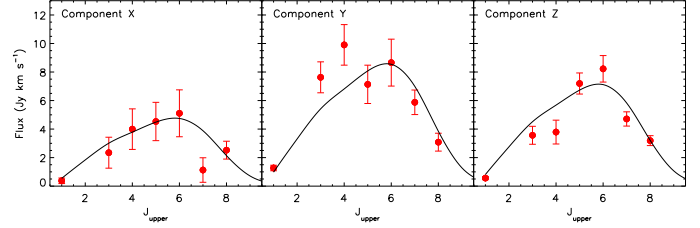


**Figure 5.** The <sup>12</sup>CO SLEDs for the three kinematic components seen within the <sup>12</sup>CO spectra (from left-to-right for the components at X, Y and Z at  $\sim -180$ , 0 and  $+200$  km s<sup>-1</sup> respectively). We overplot on each of these a scaled version of the best-fit LVG model from the combined SLED. This shows that two components, X and Z, also peak at around  $J_{\text{upper}} \sim 6$ , while component Y appears to peak slightly lower,  $J_{\text{upper}} \sim 4$ , suggesting that there may also be temperature differences between the kinematic sub-components within the galaxy. Interestingly, component Y also appears to contain the bulk of the cold gas as traced by <sup>12</sup>CO(1-0) compared to either X or Z.

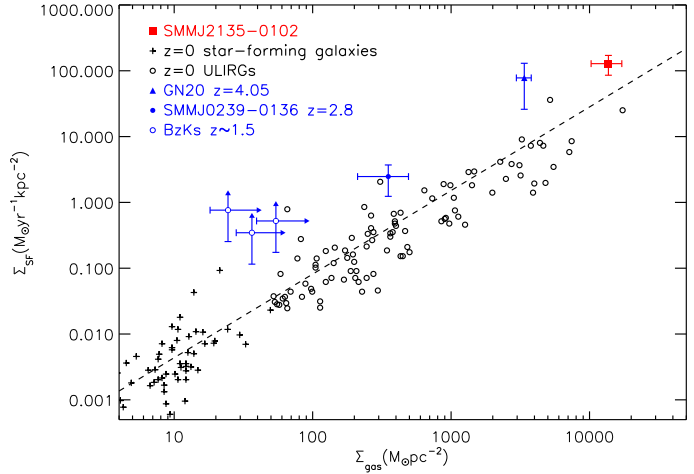


**Figure 6.** The correlation between measured gas and SFR densities for SMM J2135 compared to samples of local star-forming galaxies and ULIRGs from Kennicutt (1998) and high-redshift, as derived from <sup>12</sup>CO(1-0). The dashed line is the best fit power law to local data with  $\Sigma_{\text{SF}} \propto \Sigma_{\text{gas}}^{1.27}$  (Genzel et al. 2010). We see that the star formation within SMM J2135 is consistent with this relation assuming  $r_{\text{gas}} = r_{\text{SF}} = 1$  kpc. SMM J02399–0136 is taken from Ivison et al. (2010), GN20 from Carilli et al. 2010 and the BzKs from Aravena et al. (2010) which are unresolved in <sup>12</sup>CO(1-0), hence the arrows representing the lower limits in measured gas density.

and species. We therefore attempt to fit a model to the <sup>12</sup>CO spectra and extract <sup>12</sup>CO SLEDs for each kinematic component, in order to search for excitation structure within the system.

To construct a kinematic model for the <sup>12</sup>CO emission we fit the composite spectrum (Fig. 1) with a series of increasingly complex models. We find that a double Gaussian profile fit provides a  $\sim 14$ - $\sigma$  improvement over a single Gaussian profile, with a triple profile giving a further  $\sim 6$ - $\sigma$  improvement over the double Gaussian profile. Although this model reasonably describes the line profile of the system, P. Cox et al. (in prep) use the velocity structure from

TABLE 4: LINE RATIOS

Component	$M_{\text{H}_2+\text{He}}$ ( $10^9 M_\odot$ )	$R_{3,1}^a$	$R_{4,1}$	$R_{5,1}$	$R_{6,1}$	$R_{7,1}$	$R_{8,1}$	$\frac{L'_{\text{CI}(2-1)}}{L'_{\text{CI}(1-0)}}$	$\frac{L'_{\text{CI}(1-0)}}{L'_{\text{CO}(1-0)}}$
Total	$40.0 \pm 0.3$	$0.68 \pm 0.03$	$0.50 \pm 0.04$	$0.35 \pm 0.02$	$0.28 \pm 0.02$	$0.119 \pm 0.008$	$0.064 \pm 0.005$	$0.37 \pm 0.02$	$0.41 \pm 0.02$
Z	$10.1 \pm 1.8$	$0.71 \pm 0.19$	$0.42 \pm 0.12$	$0.51 \pm 0.11$	$0.41 \pm 0.09$	$0.17 \pm 0.04$	$0.09 \pm 0.01$	$0.85 \pm 0.21$	$0.32 \pm 0.10$
Y	$23.1 \pm 3.2$	$0.67 \pm 0.14$	$0.49 \pm 0.10$	$0.22 \pm 0.05$	$0.19 \pm 0.05$	$0.09 \pm 0.02$	$0.04 \pm 0.01$	$0.19 \pm 0.05$	$0.43 \pm 0.09$
X	$6.8 \pm 3.2$	$0.70 \pm 0.48$	$0.67 \pm 0.42$	$0.48 \pm 0.29$	$0.38 \pm 0.23$	$0.06 \pm 0.06$	$0.11 \pm 0.06$	$0.43 \pm 0.27$	$0.38 \pm 0.28$

Masses and line luminosity ratios for individual kinematic components.

<sup>a</sup> $R_{J,1}$  represents  $L'_{\text{CO}(J+1-J)}/L'_{\text{CO}(1-0)}$

high-resolution interferometry with PdBI up to  $J_{\text{upper}} = 7$  to derive a map of the dynamics of SMM J2135 on  $\sim 100$ -pc scales. The system can be described by two interacting disks: the lower-redshift of these displays a double-horned profile (termed  $Z_1$  and  $Z_2$ ), with a second,  $Y$ , at higher velocity which appears to connect to a further structure,  $X$ , extending to much higher velocity. Based on this interpretation we construct a model which comprises three components: two single Gaussians representing  $X$  and  $Y$  and a double-Gaussian for  $Z$  (constrained to have equal line widths and intensities for the two components). We fit this model to the composite spectrum, allowing the intensity, width and velocity of each component to vary and show the resulting best fit to the average line profile in Fig. 1 and report its parameters in Table 3. This fit has a  $\chi^2$  of  $\sim 20$  for seven degrees of freedom and provides an adequate description of the composite line profile.

Using the best-fit model parameters from the composite  $^{12}\text{CO}$  spectrum, we apply the fit to each  $^{12}\text{CO}$  spectrum in turn, in order to extract the SLEDs for the three components in the model. Beginning with the average model parameters, we perturb the best fit randomly by up to  $\pm 20 \text{ km s}^{-1}$  and fit this new realisation to each of the  $^{12}\text{CO}$  spectra in turn, allowing only the relative intensities of the components to vary. We then sum the  $\chi^2$  for the fit to each line for each model and determine the parameters for which the total  $\chi^2$  is a minimum. We show the best fit model's line profile on each line in Fig. 1 and report their parameters in Table 3. To calculate errors, we allow the best fit parameters of the kinematic model to randomly vary (by their  $1\text{-}\sigma$  uncertainties) and run  $10^5$  Monte Carlo simulations, determining the  $1\text{-}\sigma$  variance in the range of fluxes from those models where the total  $\chi^2$  of the model fit is within  $\Delta\chi^2 = 21$  of the best fit (since we have seven emission lines and fit with three free parameters to each line). The errors on the parameters for the model fit to the average (velocity and dispersion in Table 3) are calculated using the standard deviation of the parameters for all models for which the total  $\chi^2$  of the model fit is within  $\Delta\chi^2 = 21$  of the best fit; these are quoted in Table 3.

The  $^{12}\text{CO}$  SLEDs for the three individual components are shown in Fig. 5. We derive the gas masses for each component using the  $^{12}\text{CO}(1-0)$  emission line and assuming our effective conversion factor  $\alpha = 2.0$  and list these in Table 4. The most highly excited components are  $X$  and  $Z$ , peaking at  $J_{\text{upper}} \sim 6$ , and containing  $\sim 15\%$  and  $\sim 25\%$  of total gas mass respectively (Table 4). Component  $Y$ , which we

associate with the core of the second interacting system, is somewhat less excited, peaking at  $J_{\text{upper}} \sim 4$ , and contains most of the gas in the system ( $\sim 60\%$  of the total gas mass and a majority of the cold gas).

For each of the SLEDs, we perform further LVG modelling as applied to the combined spectrum. However, within the errors, we cannot measure any temperature difference between the three components although there is a hint that  $Y$  is cooler than  $X$  or  $Z$ . However, while the  $[\text{Cl}](^3P_2 \rightarrow ^3P_1)$  and  $[\text{Cl}](^3P_1 \rightarrow ^3P_0)$  lines have lower signal-to-noise than the  $^{12}\text{CO}$  lines, we can also decompose them using the same method. Table 4 shows the ratio of  $L'_{[\text{Cl}](^3P_2 \rightarrow ^3P_1)}/L'_{[\text{Cl}](^3P_1 \rightarrow ^3P_0)}$  for the different components, with  $Z$  having the largest ratio and  $Y$  having the smallest. The corresponding excitation temperatures are  $T_{\text{ex}} > 100 \text{ K}$ ,  $T_{\text{ex}} = 24.7 \pm 0.5 \text{ K}$  and  $T_{\text{ex}} = 52.5 \pm 6.3 \text{ K}$  for  $Z$ ,  $Y$  and  $X$  respectively (where the temperature calculated for the  $Z$  component may be discrepant and likely caused by a problem with the model fit to the line; see Fig. 1). This supports the suggestion from the  $^{12}\text{CO}$  SLED that both  $X$ , and especially  $Z$ , are hotter than the more massive  $Y$ .

### 3.4 Physical Interpretation

Swinbank et al. (2010) show that the rest-frame  $\sim 250\text{-}\mu\text{m}$  emission from SMM J2135 is concentrated in four bright, star-forming regions each of which has a radius of  $\sim 100 \text{ pc}$  spread across a more diffuse structure with a total extent of  $2 \text{ kpc}$  in projection. Following this we fitted the integrated dust SED of the source (see §3.1.1) assuming that  $\sim 20\%$  of the  $870\text{-}\mu\text{m}$  flux is coming from a relatively cool ( $T_d \sim 30 \text{ K}$ ) extended dust component with a predicted radius of  $\sim 1 \text{ kpc}$  and  $\sim 80\%$  emerges from the four  $\sim 100\text{-pc}$  radius, hotter ( $T_d \sim 60 \text{ K}$ ) and optically thick, clumps. Our modelling of both the  $^{12}\text{CO}$  SLED and the kinematically decomposed  $[\text{Cl}]$  line ratios supports the presence of two phases in the ISM within this galaxy with a cool,  $15\text{--}25 \text{ K}$ , phase and a hotter,  $45\text{--}60 \text{ K}$  phase (although it is likely that these actually represent a continuum of properties). We also find an enhancement in the  $[\text{Cl}]/^{12}\text{CO}$  ratio (likely due to low metallicity and/or higher cosmic ray flux) which is associated with the cool phase in this system. Our kinematic model identifies a component  $Y$  which is relatively cool and contains the about half of the gas in the system, while the hotter material is more closely tied to component  $Z$  (and to a lesser extent  $X$ ). It is tempting to associate these kinematic components with the clumps seen in the SMA map,

but as we discuss below, it is more likely that the clumps lie within these kinematic structures, rather than having a unique one-to-one relationship.

Our observations also provide other limits on the characteristic size and morphology for the emission regions. We can use the characteristic density derived from the PDR analysis, together with the total gas mass to derive an effective radius of the system. Adopting  $M(\text{H}_2+\text{He}) \sim 4 \times 10^{10} M_\odot$  and a density of  $\sim 10^4 \text{ cm}^{-3}$  from the Kaufman et al. (1999) models, we derive the radius of an equivalent sphere of  $\sim 300 \text{ pc}$  (or  $\sim 700 \text{ pc}$  for a disk with a thickness of  $\sim 100 \text{ pc}$ ). These sizes are larger than the clump sizes in the sub-millimetre, which again is consistent with the interpretation from the LVG modelling that the  $^{12}\text{CO}$  is much more wide spread than the star-forming clumps. If we similarly split the gas mass into four equal clumps, then the expected sizes of these are  $\sim 200 \text{ pc}$  in radius, which is slightly larger than the far-infrared sizes of the star-forming regions within SMM J2135.

We can also use the value of  $G_0 \sim 10^{3.6}$  Habing fields, as determined from the PDR models, to estimate the characteristic size of the galaxy. Assuming a Salpeter IMF and a constant SFR in the burst then the ionising flux (6–13.6 eV) is  $\sim 50\%$  of the bolometric luminosity for ages of 10–100 Myrs. We can determine the size of a region where the typical ionising field, as estimated from our bolometric luminosity, equals  $G_0$ . This gives an estimate for the system’s radius of  $\sim 1 \text{ kpc}$ , similar to the characteristic size inferred from the LVG modelling of the dust SED and the overall extent of the system from the SMA observations.

We can use the kinematics of the components and the potential sizes and estimate the gas mass fractions in these various components. We first note that the dynamical mass of a uniform sphere with velocity dispersion of  $\sigma \sim 75\text{--}160 \text{ km s}^{-1}$  (Table 3) and an effective radius of  $r \sim 200\text{--}1000 \text{ pc}$  is  $\sim 0.1\text{--}3 \times 10^{10} M_\odot$ . The gas masses from Fig. 5 (using  $\alpha = 2.0$ ) are  $\sim 7\text{--}23 \times 10^9 M_\odot$ , similar to the range of dynamical masses, indicating that the gas reservoirs in these components must have effective radii comparable to the estimates above from the various size indicators. This also shows that we cannot significantly increase  $\alpha$ , for example to the Milky Way value of  $\alpha \sim 4.6$ , since this would result in a range of gas masses of  $\sim 1.4\text{--}4.7 \times 10^{10} M_\odot$ , in excess of the dynamical masses unless the gas has disk-like kinematics and we are seeing these almost face on, which is unlikely given the large velocity dispersion.

Our size estimates for the gas reservoirs are larger than the size of the clumps in the SMA map and are more comparable to the extent of the whole system, which suggests that the cold gas is more widely distributed than the  $\lesssim 100\text{-pc}$  radius far-infrared clumps. Thus, these clumps are likely to be knots of emission lying within a colder and more extended structure. Although the clumps will trace the kinematics of the gas in which they are embedded, they may not represent the deepest parts of the potential well, and so the star formation may be free to migrate around the gas reservoir. These intense star-forming regions have crossing times of just a few Myrs and they have free-fall SFRs (Krumholz & Tan 2007) of  $\sim 0.001$  indicating that they are supported against collapse (most likely by internal turbulence).

Finally, with an estimate of the overall extent of the gas reservoir, we investigate where SMM J2135 lies on the

Kennicutt-Schmidt relation, which links the star-formation and gas surface density ( $\Sigma_{\text{SFR}}$  and  $\Sigma_{\text{gas}}$  respectively). This relation is approximately linear up to a threshold of  $\sim 0.1 M_\odot \text{ pc}^{-2}$ , above which the density of the ISM becomes dominated by molecular gas and the star-formation law instead follows  $\Sigma_{\text{SFR}} \propto \Sigma_{\text{gas}}^{1.4}$  (Kennicutt 1998). Previous work has shown broad universality of this relation with redshift, although at  $z \sim 2$ , both surface brightness and instrument limitations mean that a direct comparison to low-redshift galaxies has been difficult, with extrapolations from high-J CO in intrinsically luminous galaxies providing most constraints (e.g. Genzel et al. 2010). Some of this tension can be alleviated by using the CO(1–0) emission (or LVG modelling of the full CO SLED) to provide a more reliable estimate of the gas mass and spatial extent, and in Fig. 6 we show the Kennicutt-Schmidt relation and overlay the position of SMM J2135. We also include on the plot the high-redshift galaxies where CO(1–0) observations are available. This figure shows that SMM J2135 lies at the high star-formation and gas-density end of the correlation, although within the scatter seen for local ULIRGs.

Although we do not have spatially resolved spectroscopy to probe the gas properties on  $\sim 100 \text{ pc}$  scales, we can ask where the individual star-forming regions would lie if they too followed the Kennicutt-Schmidt relation. Assuming that 80% of the bolometric luminosity arises in these clumps, and that each clump has a radius of  $r_{\text{SF}}=r_{\text{gas}} \sim 100 \text{ pc}$ , then the inferred gas density would be  $n \sim 3 \times 10^5 \text{ cm}^{-2}$ , which is substantially higher than that inferred from the PDR and LVG modelling of the dense gas tracers ( $n \sim 10^{3.5\text{--}4.5} \text{ cm}^{-2}$ ). However, taking the remaining 20% of the bolometric luminosity with a radius of  $1 \text{ kpc}$  (and assuming the gas lies in an extended disk), the density is  $n \sim 0.2\text{--}1 \times 10^4 \text{ cm}^{-2}$  (with the main uncertainty being the disk thickness). Thus, although this calculation should be considered crude, the results are consistent with a model in which the sub-millimetre emission predominantly traces the star-forming clumps on  $\sim 100 \text{ pc}$  scales, but these clumps are simply embedded in a much more extended structure which dominates the  $^{12}\text{CO}$  emission. These results may also imply a break-down of the Kennicutt-Schmidt relation on scales of individual GMCs ( $< 100 \text{ pc}$ , see also Onodera et al. 2010) although clearly high resolution millimetre observations would accurately constrain their sizes, which is a fundamental step in understanding the conditions within the ISM of high-redshift galaxies (P. Cox et al. in prep).

## 4 CONCLUSIONS

We have presented detections of a number of rest-frame, far-infrared and sub-millimetre molecular and atomic emission lines in the spectrum of the lensed sub-millimetre galaxy SMM J2135. We have used these lines to construct the  $^{12}\text{CO}$  SLED up to  $J_{\text{upper}} = 10$  and analysed this and the other species, including the HCN(3–2) and [C I] fine structure lines, to investigate the physical conditions within the interstellar medium in this galaxy. Our main results are:

The  $^{12}\text{CO}$  SLED resembles that of local starburst galax-

ies. An LVG analysis of the  $^{12}\text{CO}$  SLED shows at least two phases with temperatures  $T \sim 25$  and  $60\text{ K}$ .

The dust SED is best fit by a model in which the galaxy comprises an extended component with radius  $\sim 1\text{--}2\text{ kpc}$  with  $T_d \sim 30\text{ K}$  and four high-density, star-forming regions with sizes of order  $r \sim 200\text{ pc}$  and  $T_d \sim 60\text{ K}$ . These characteristics are roughly consistent with the rest-frame  $\sim 250\text{-}\mu\text{m}$  morphology of the system as seen by SMA and the two components may link to the phases identified from the  $^{12}\text{CO}$  SLED. At  $J_{\text{upper}} = 1\text{--}0$ , the cooler, diffuse phase appears to comprise 50% of the molecular gas. We also derive a carbon mass of  $M_{\text{CI}} = (9.1 \pm 0.2) \times 10^6 M_{\odot}$  and hence a carbon abundance of  $\sim 4 \times 10^{-5}$  which is slightly above the Galactic value. LVG modelling suggests that the dense, star-forming regions have abundances similar to that seen in the Milky Way, whilst the extended diffuse gas has lower metallicity (or a higher cosmic ray flux).

Using the  $^{12}\text{CO}$  emission and assuming  $\alpha = 0.8$  we estimate the total molecular gas mass from the  $^{12}\text{CO}(1\text{--}0)$  emission as  $M(\text{H}_2) = (1.4 \pm 0.1) \times 10^{10} M_{\odot}$ . Comparing this with that derived from  $J_{\text{upper}} \geq 3$  transitions, assuming thermalised gas, shows that these predicted gas masses are a factor  $1.5\text{--}3.6\times$  too low, indicative of multiple gas phases, as seen in local starbursts. However, our LVG analysis indicates a higher gas mass,  $M(\text{H}_2) \sim 4 \times 10^{10} M_{\odot}$ , yielding an effective CO-to- $\text{H}_2$  conversion factor of  $\alpha \sim 2.0$ . If these conditions are relevant in the wider SMG population then this suggests that previous,  $J_{\text{upper}} \geq 3$   $^{12}\text{CO}$  observations of SMGs may have underestimated the molecular gas content of SMGs by at least a factor of  $\sim 2\text{--}5\times$  (see also Ivison et al. 2010; Harris et al. 2010).

Within SMM J2135 we detect the  $\text{HCN}(3\text{--}2)$  emission at the  $3\text{-}\sigma$  level, and use this to estimate a dense gas mass of  $M_{\text{dense}}(\text{H}_2) = \alpha_{\text{HCN}} L'_{\text{HCN}} < 4.5 \times 10^{10} M_{\odot}$  assuming  $\alpha_{\text{HCN}} = 10$  (Gao & Solomon 2004). Within the uncertainties in  $\alpha_{\text{HCN}}$  this is consistent with the gas mass derived from  $^{12}\text{CO}$ , indicating that HCN may be a promising route to constraining the dense gas masses of high-redshift galaxies in the future (Gao et al. 2007), particularly if two or more HCN lines are measured. We also find that the  $\text{HCN}/\text{FIR}$  ratio is consistent with that of local ULIRGs and star-forming galaxies with no evidence for AGN contribution to the FIR luminosity.

We use the atomic fine-structure and molecular line ratios to investigate the excitation conditions within the ISM, and find that they are similar to those found in local starbursts and ULIRGs. Using a grid of PDR models, we show that the molecular gas in SMM J2135 is exposed to a UV radiation field which is  $\sim 1000\times$  more intense than that of the Milky Way, and has a density of  $n \sim 10^4\text{ cm}^{-3}$ , both characteristic of the central regions of a typical starburst galaxy. Thus, the inferred density and far-UV radiation field strength of the ISM appear similar to those seen in local ULIRGs consistent with the interpretation of SMGs as the high-redshift analogs of these merger-driven starbursts. However, the spatial extent and mass of the gas reservoir (and spatial extent of the star formation) is larger than typically found in local ULIRGs.

We find that the  $^{12}\text{CO}$  emission shows multiple kinematic components and we decompose the SLEDs into three kinematic components to investigate the excitation variations within the system. We find tentative evidence of tem-

perature variation between the kinematic components, although we defer a detailed discussion of the kinematics to a future paper (P. Cox et al. in prep).

Using a number of approaches we have derived estimates for the effective size of the gas reservoir within this system. All of our estimates are larger than the size of the clumps detected in the  $870\text{-}\mu\text{m}$  map from SMA, implying that the gas traces a more extended structure. Overall, our modelling of the  $^{12}\text{CO}$  SLED supports the presence of two phases in the ISM, with one phase associated with  $\sim$ solar metallicity star-forming clumps with  $> 100\text{ pc}$  sizes, embedded in a low metallicity (or high cosmic ray flux), extended component with a characteristic size of  $\sim 1\text{ kpc}$ . However, even the “extended” component has a much higher gas density than typically observed in local starbursts such as M 82 (although a similar density to local ULIRGs such as Arp 220), and is exposed to a UV radiation field which is  $\sim 1000\times$  more intense than the Milky Way (Gerin & Phillips 1998).

Assuming that the molecular gas is evenly distributed, we show that the integrated properties of the galaxy follow the Kennicutt-Schmidt relation. We also test where the individual star-forming regions would lie if they too followed the Kennicutt-Schmidt relation, and we show that on  $\sim 100\text{ pc}$  scales, the gas density would be  $\sim 30\times$  higher than that inferred from the LVG or PDR analysis. However, the properties of the diffuse gas disk suggest a characteristic density  $n \sim 0.2\text{--}1 \times 10^4\text{ cm}^{-3}$ , which is comparable to that inferred from the LVG and PDR models. These results are consistent with a model in which the sub-millimetre emission predominantly traces the dense cores of the star-forming regions, but that these clumps are simply embedded in a much more extended and diffuse structure which dominates the gas emission. These results may also imply a break-down of the Kennicutt-Schmidt relation on scales of individual GMCs (e.g.  $< 100\text{ pc}$ ), although clearly only high-resolution millimetre observations will accurately constrain their sizes.

These results show that it is possible to unravel the complex ISM physics within starburst galaxies at high redshift at a level of detail which, until recently has only been possible in the  $z < 0.1$  Universe. Our observations provide an unique window into the physics of star-formation at  $z \sim 2$  with signal-to-noise that would otherwise require the increased light grasp of the next generation facilities. Indeed this source provides insight into the science that will be routinely possible once ALMA reaches full science operations.

## ACKNOWLEDGMENTS

ALRD acknowledges an STFC studentship, AMS gratefully acknowledges a Sir Norman Lockyer Royal Astronomical Society Fellowship, IRS acknowledges support from STFC. We are very grateful to Padelis Papadopoulos for extensive discussion and comments on this manuscript. We also thank Estelle Bayet, Carsten Kramer, Rowin Meijerink, Serena Viti, Paul van der Werf and Chris Wilson for a number of useful discussions. We thank the anonymous referee for useful comments which added to the clarity and content of this paper. The observations in this paper were carried out with the IRAM 30m and the Plateau de Bure Interferometer.



IRAM is supported by INSU/CNRS (France), MPG (Germany) and IGN (Spain). We also thank the ESO Director for generously granting DDT observations with SHFI as part of program 283.A-5014 which is based on data acquired with the Atacama Pathfinder Experiment (APEX). APEX is a collaboration between the Max-Planck-Institut für Radioastronomie, the European Southern Observatory, and the Onsala Space Observatory. The Submillimeter Array is a joint project between the Smithsonian Astrophysical Observatory and the Academia Sinica Institute of Astronomy and Astrophysics and is funded by the Smithsonian Institution and the Academia Sinica. Zpectrometer observations were taken as part of program 09A-040. Zpectrometer is supported by National Science Foundation grants AST-0503946 and AST-070865, and by the National Radio Astronomy Observatory. The National Radio Astronomy Observatory is a facility of the National Science Foundation operated under cooperative agreement by Associated Universities, Inc.

## REFERENCES

- Aalto S., Booth R. S., Black J. H., Johansson L. E. B., 1995, *A&A*, 300, 369
- Aravena M., Carilli C., Daddi E., Wagg J., Walter F., Riechers D., Dannerbauer H., Morrison G. E., Stern D., Krips M., 2010, *ApJ*, 718, 177
- Baker A. J., Tacconi L. J., Genzel R., Lehnert M. D., Lutz D., 2004, *ApJ*, 604, 125
- Bayet E., Gerin M., Phillips T. G., Contursi A., 2004, *A&A*, 427, 45
- Bayet E., Gerin M., Phillips T. G., Contursi A., 2006, *A&A*, 460, 467
- Bennett C. L., Fixsen D. J., Hinshaw G., Mather J. C., Moseley S. H., Wright E. L., Eplee, Jr. et al 1994, *ApJ*, 434, 587
- Blain A. W., Smail I., Ivison R. J., Kneib J.-P., Frayer D. T., 2002, *PhR*, 369, 111
- Bolatto A. D., Jackson J. M., Kraemer K. E., Zhang X., 2000, *ApJL*, 541, L17
- Bradford C. M., Nikola T., Stacey G. J., Bolatto A. D., Jackson J. M., Savage M. L., Davidson J. A., Higdon S. J., 2003, *ApJ*, 586, 891
- Brown W. R., Kewley L. J., Geller M. J., 2008, *AJ*, 135, 92
- Bryant P. M., Scoville N. Z., 1996, *ApJ*, 457, 678
- Carilli C. L., Daddi E., Riechers D., Walter F., Weiss A., Dannerbauer H., Morrison G. E., Wagg, J et al. 2010, *ApJ*, 714, 1407
- Coppin K. E. K., Swinbank A. M., Neri R., Cox P., Smail I., Ellis R. S., Geach J. E., Siana et al. 2007, *ApJ*, 665, 936
- Davé R., Finlator K., Oppenheimer B. D., Fardal M., Katz N., Kereš D., Weinberg D. H., 2010, *MNRAS*, 404, 1355
- Davies R. I., Sternberg A., Lehnert M., Tacconi-Garman L. E., 2003, *ApJ*, 597, 907
- Devereux N., Taniguchi Y., Sanders D. B., Nakai N., Young J. S., 1994, *AJ*, 107, 2006
- Downes D., Solomon P. M., 1998, *ApJ*, 507, 615
- Flower D. R., 2001, *MNRAS*, 328, 147
- Flower D. R., Le Bourlot J., Pineau Des Forets G., Roueff E., 1994, *A&A*, 282, 225
- Frayer D. T., Ivison R. J., Scoville N. Z., Evans A. S., Yun M. S., Smail I., Barger A. J., Blain A. W., Kneib J.-P., 1999, *ApJL*, 514, L13
- Frayer D. T., Ivison R. J., Scoville N. Z., Yun M., Evans A. S., Smail I., Blain A. W., Kneib J., 1998, *ApJL*, 506, L7
- Frerking M. A., Keene J., Blake G. A., Phillips T. G., 1989, *ApJ*, 344, 311
- Gao L., Springel V., White S. D. M., 2005, *MNRAS*, 363, L66
- Gao Y., Carilli C. L., Solomon P. M., Vanden Bout P. A., 2007, *ApJL*, 660, L93
- Gao Y., Solomon P. M., 2004, *ApJ*, 606, 271
- Genzel R., Tacconi L. J., Gracia-Carpio J., Sternberg A., Cooper M. C., Shapiro K., Bolatto A., Bouche N., Bournaud F., Burkert, A., et al. 2010, *ArXiv e-prints*
- Gerin M., Phillips T. G., 1998, *ApJL*, 509, L17
- Gerin M., Phillips T. G., 2000, *ApJ*, 537, 644
- González-Alfonso E., Fischer J., Isaak K., Rykala A., Savini G., Spaans M., van der Werf P., Meijerink, R. et al 2010, *ArXiv e-prints*
- Greve T. R., Bertoldi F., Smail I., Neri R., Chapman S. C., Blain A. W., Ivison R. J., Genzel et al. 2005, *MNRAS*, 359, 1165
- Greve T. R., Ivison R. J., Papadopoulos P. P., 2003, *ApJ*, 599, 839
- Greve T. R., Papadopoulos P. P., Gao Y., Radford S. J. E., 2009, *ApJ*, 692, 1432
- Guesten R., Serabyn E., Kasemann C., Schinckel A., Schneider G., Schulz A., Young K., 1993, *ApJ*, 402, 537
- Hailey-Dunsheath S., Nikola T., Stacey G. J., Oberst T. E., Parshley S. C., Benford D. J., Staguhn J. G., Tucker C. E., 2010a, *ApJL*, 714, L162
- Hailey-Dunsheath S., Nikola T., Stacey G. J., Oberst T. E., Parshley S. C., Benford D. J., Staguhn J. G., Tucker C. E., 2010b, *ApJL*, 714, L162
- Harris A. I., Baker A. J., Jewell P. R., Rauch K. P., Zonak S. G., O’Neil K., Shelton A. L., Norrod, R. et al., 2007, in A. J. Baker, J. Glenn, A. I. Harris, J. G. Mangum, & M. S. Yun ed., *From Z-Machines to ALMA: (Sub)Millimeter Spectroscopy of Galaxies* Vol. 375 of ASPC, The Zpectrometer: an Ultra-Wideband Spectrometer for the Green Bank Telescope. p. 82
- Harris A. I., Baker A. J., Zonak S. G., Sharon C. E., Genzel R., Rauch K., Watts G., Creager R., 2010, *ArXiv e-prints*
- Harrison A., Puxley P., Russell A., Brand P., 1995, *MNRAS*, 277, 413
- Hocuk S., Spaans M., 2010, *A&A*, 510, A110+
- Israel F. P., Baas F., 2002, *A&A*, 383, 82
- Israel F. P., Maloney P. R., Geis N., Herrmann F., Madden S. C., Poglitsch A., Stacey G. J., 1996, *ApJ*, 465, 738
- Israel F. P., White G. J., Baas F., 1995, *A&A*, 302, 343
- Ivison R. J., Smail I., Papadopoulos P. P., Wold I., Richard J., Swinbank A. M., Kneib J., Owen F. N., 2010, *MNRAS*, 404, 198
- Ivison R. J., Swinbank A. M., Swinyard B., Smail I., Pearson C. P., Rigopoulou D., Polehampton E., Baluteau, J.-P. et al. 2010, *A&A*, 518, L35
- Juneau S., Narayanan D. T., Moustakas J., Shirley Y. L., Bussmann R. S., Kennicutt R. C., Vanden Bout P. A., 2009, *ApJ*, 707, 1217
- Kaufman M. J., Wolfire M. G., Hollenbach D. J., Luhman

- M. L., 1999, *ApJ*, 527, 795
- Kennicutt Jr. R. C., 1998, *ApJ*, 498, 541
- Kramer C., Cubick M., Röllig M., Sun K., Yonekura Y., Aravena M., Bensch F., Bertoldi, F. et al. 2008, *A&A*, 477, 547
- Kramer C., Jakob H., Mookerjee B., Schneider N., Brüll M., Stutzki J., 2004, *A&A*, 424, 887
- Krumholz M. R., Tan J. C., 2007, *ApJ*, 654, 304
- Maiolino R., Caselli P., Nagao T., Walmsley M., De Breuck C., Meneghetti M., 2009, *A&A*, 500, L1
- Malhotra S., Kaufman M. J., Hollenbach D., Helou G., Rubin R. H., Brauer J., Dale D., Lu, N. Y. et al 2001, *ApJ*, 561, 766
- Mao R. Q., Henkel C., Schulz A., Zielinsky M., Mauersberger R., Störzer H., Wilson T. L., Gensheimer P., 2000, *A&A*, 358, 433
- Meijerink R., Spaans M., Israel F. P., 2007, *A&A*, 461, 793
- Negishi T., Onaka T., Chan K., Roellig T. L., 2001, *A&A*, 375, 566
- Onodera S., Kuno N., Tosaki T., Kohno K., Nakanishi K., Sawada T., Muraoka K., Komugi, S. et al. 2010, *ArXiv e-prints*
- Panuzzo P., Rangwala N., Rykala A., Isaak K. G., Glenn J., Wilson C. D., Auld R., Baes, M. et al. 2010, *ArXiv e-prints*
- Papadopoulos P. P., 2007, *ApJ*, 656, 792
- Papadopoulos P. P., Greve T. R., 2004, *ApJL*, 615, L29
- Papadopoulos P. P., Isaak K. G., van der Werf P. P., 2007, *ApJ*, 668, 815
- Papadopoulos P. P., Thi W., Viti S., 2004, *MNRAS*, 351, 147
- Papadopoulos P. P., van der Werf P., Isaak K., Xilouris E. M., 2010, *ApJ*, 715, 775
- Pety J., 2005, in F. Casoli, T. Contini, J. M. Hameury, & L. Pagani ed., *SF2A-2005: Semaine de l'Astrophysique Française Successes of and Challenges to GILDAS, a State-of-the-Art Radioastronomy Toolkit*. p. 721
- Pineda J. L., Bensch F., 2007, *A&A*, 470, 615
- Sakamoto K., Scoville N. Z., Yun M. S., Crosas M., Genzel R., Tacconi L. J., 1999, *ApJ*, 514, 68
- Scoville N., 2004, in S. Aalto, S. Huttemeister, & A. Pedlar ed., *The Neutral ISM in Starburst Galaxies Vol. 320 of ASPC, Starburst and AGN Connections*. pp 253+
- Scoville N. Z., Yun M. S., Bryant P. M., 1997, *ApJ*, 484, 702
- Smail I., Ivison R. J., Blain A. W., Kneib J.-P., 2002, *MNRAS*, 331, 495
- Socrates A., Davis S. W., Ramirez-Ruiz E., 2008, *ApJ*, 687, 202
- Solomon P. M., Vanden Bout P. A., 2005, *ARAA*, 43, 677
- Spaans M., 1996, *A&A*, 307, 271
- Spaans M., Meijerink R., 2008, *ApJL*, 678, L5
- Spergel D. N., Verde L., Peiris H. V., Komatsu E., Nolte M. R., Bennett C. L., Halpern M., Hinshaw, G., et al. 2003, *APJS*, 148, 175
- Stacey G. J., Geis N., Genzel R., Lugten J. B., Poglitsch A., Sternberg A., Townes C. H., 1991, *ApJ*, 373, 423
- Stark A. A., Bolatto A. D., Chamberlin R. A., Lane A. P., Bania T. M., Jackson J. M., Lo K., 1997, *ApJL*, 480, L59
- Stark D. P., Swinbank A. M., Ellis R. S., Dye S., Smail I. R., Richard J., 2008, *Nature*, 455, 775
- Stutzki J., Graf U. U., Haas S., Honingh C. E., Hottgenroth D., Jacobs K., Schieder R., Simon, R. et al 1997, *ApJL*, 477, L33
- Swinbank A. M., Smail I., Longmore S., Harris A. I., Baker A. J., De Breuck C., Richard J., Edge, A. C. et al 2010, *Nature*, 464, 733
- Tacconi L. J., Genzel R., Smail I., Neri R., Chapman S. C., Ivison R. J., Blain A., Cox et al. 2008, *ApJ*, 680, 246
- Tacconi L. J., Neri R., Chapman S. C., Genzel R., Smail I., Ivison R. J., Bertoldi F., Blain et al. 2006, *ApJ*, 640, 228
- Teyssier R., Chapon D., Bournaud F., 2010, *ArXiv e-prints*
- Thompson T. A., Quataert E., Murray N., 2005, *ApJ*, 630, 167
- van der Werf P. P., Isaak K. G., Meijerink R., Spaans M., Rykala A., Fulton T., Loenen A. F., Walter, F 2010, *ArXiv e-prints*
- Vassilev V., Meledin D., Lapkin I., Belitsky V., Nyström O., Henke D., Pavolotsky A., Monje, R. et al. 2008, *A&A*, 490, 1157
- Walter F., Riechers D., Cox P., Neri R., Carilli C., Bertoldi F., Weiss A., Maiolino R., 2009, *Nature*, 457, 699
- Ward J. S., Zmuidzinas J., Harris A. I., Isaak K. G., 2003, *ApJ*, 587, 171
- Weiß A., Downes D., Henkel C., Walter F., 2005, *A&A*, 429, L25
- Weiß A., Downes D., Neri R., Walter F., Henkel C., Wilner D. J., Wagg J., Wiklind T., 2007, *A&A*, 467, 955
- Weiß A., Downes D., Walter F., Henkel C., 2005, *A&A*, 440, L45
- Weiß A., Walter F., Scoville N. Z., 2005, *A&A*, 438, 533
- White G. J., Ellison B., Claude S., Dent W. R. F., Matheson D. N., 1994, *A&A*, 284, L23
- Wild W., Harris A. I., Eckart A., Genzel R., Graf U. U., Jackson J. M., Russell A. P. G., Stutzki J., 1992, *A&A*, 265, 447
- Young J. S., Scoville N. Z., 1984, *ApJ*, 287, 153
- Yuan T., Kewley L. J., 2009, *ApJL*, 699, L161
- Zmuidzinas J., Betz A. L., Boreiko R. T., Goldhaber D. M., 1988, *ApJ*, 335, 774